Effective Seismic Force Retrieval from Surface Measurement for SH-Wave Reconstruction

Bruno Guidio[a], Heedong Goh[b,c], Chanseok Jeong[a,d,*]

[a] School of Engineering and Technology, Central Michigan University, Mount Pleasant, 48859, MI, USA
[b] Department of Electrical and Computer Engineering, The University of Texas at Austin, Austin, 78712, TX, USA
[c] Photonics Initiative, Advanced Science Research Center, City University of New York, New York, 10031, NY, USA
[d] Earth and Ecosystem Science Program, Central Michigan University, Mount Pleasant, 48859, MI, USA

Abstract

We present a new method to obtain dynamic body force at virtual interfaces to reconstruct shear wave motions induced by a source outside a truncated computational domain. Specifically, a partial differential equation (PDE)-constrained optimization method is used to minimize the misfit between measured motions at a limited number of sensors on the ground surface and their counterparts reconstructed from optimized forces. Numerical results show that the optimized forces accurately reconstruct the targeted ground motions in the surface and the interior of the domain. The proposed optimization framework yields a particular force vector among other valid solutions allowed by the domain reduction method (DRM). Per this optimized or inverted force vector, the reconstructed wave field is identical to its reference counterpart in the domain of interest but may differ in the exterior domain from the reference one. However, we remark that the inverted solution is valid and introduce a simple post-process that can modify the solution to achieve an alternative force vector corresponding to the reference wave field. We also study the desired sensor spacing to accurately reconstruct the wave responses for a given dominant frequency of interest. We remark that the presented method is omnidirectionally applicable in terms of the incident angle of an incoming wave and is effective for any given material heterogeneity and geometry of layering of a reduced domain. The presented inversion method requires information on the wave speeds and dimensions of only a reduced domain. Namely, it does not need any information on the geophysical profile of an enlarged domain or a seismic source profile outside a reduced domain. Thus, the computational cost of the method is compact even though it leads to the high-fidelity reconstruction of wave response in the reduced domain, allowing for studying and predicting ground and structural responses using real seismic measurements.

Keywords: Passive-seismic inversion, Domain reduction method (DRM), Effective seismic force vector, Discretize-then-optimize (DTO) approach, Reconstruction of seismic responses, Full-waveform inversion.

1. Introduction

The ability to replay the wave motions from sparsely-measured ground motion data is of great interest to identify the locations of large-amplitude dynamic responses during a seismic event. Such technique allows engineers to accurately estimate earthquakes' impact on soils and critical structures (e.g., tunnels, subways, bridges, power plants, dams, lifelines, tall buildings) and weak or potentially-damaged spots in the structures. This information on seismic impact estimation could be shared with decision-makers who would determine the budget and timeline to inspect and fix the seismic damages of built environments.

Thus, engineers should be able to identify seismic sources from the measured ground-motion data to reconstruct the corresponding seismic responses in the domain of interest. Although a large amount of ground motion data are available from modern sensors, such as accelerometers, optical cables, distributed acoustic sensing (DAS), and vision

*Corresponding author
Email address: jeong1c@cmich.edu (Chanseok Jeong)

sensors, there is no established method to identify arbitrarily-incoherent incident wave motions and to reconstruct the corresponding responses in a truncated multi-dimensional near-surface domain.

Common methods to identify earthquake waves hitting a domain of consideration include 1) deconvolution in a soil column and 2) seismic source identification in an extensive regional-scale domain. The deconvolution algorithm allows engineers to identify an incident earthquake wave signal propagating into a 1D soil domain from surficial seismic measurement [1, 2, 3]. However, the method is useful only when geophysical property is horizontally layered and incoming seismic waves propagate vertically through the 1D columns. Thus, the approach fails to reconstruct the incoming waves when the geophysical property is highly heterogeneous, rather than horizontally layered, and incident earthquake waves—consisting of primary, shear, and surface waves—are not vertically propagating (i.e., incoherent) due to the basin effect. In the same context, Mena and Jeremic [4] have confirmed the substantial difference between (*i*) the seismic structural responses from the domain reduction method (DRM)-based seismic wave analysis using "true" 3D incoherent free-field wave motions and (*ii*) their counterparts using 1D vertically-propagating free-field motions that are generated by the deconvolution from measured ground motions. On the other conventional method, there have been studies on a regional-scale inversion of seismic-source parameters at a hypocenter. For instance, Akcelik et al. [5] studied an algorithm to invert a simplified seismic source time signal in a large regional-scale 3D domain that includes a source at a fault. However, the uncertainties in material properties in a large domain hinder the method, and, more importantly, its computational cost is too high to simulate high-frequency contents (e.g., $f > 1$ Hz) of ground wave motions. Because of the applicability and computational limits of the two conventional approaches stated above, it is necessary to investigate an alternative method to identify arbitrarily-incoherent (due to, for instance, the basin effect) incoming seismic waves or equivalent dynamic forces and reconstruct corresponding ground motions within a 2D/3D reduced domain from observational data of seismic waves at sensors.

Several recent studies in the literature have reported the possibility of utilizing sparsely measured wave motion data to estimate unknown earthquake waves entering a solid domain via a full-waveform inversion technique, which has been widely used in geotechnical site characterization [6, 7, 8, 9, 10, 11, 12, 13, 14]. First, Jeong and Seylabi [15] studied an inversion procedure for predicting an incoming earthquake wave in a one-dimensional soil column. Guidio and Jeong [16] discussed an inversion process to estimate the function of targeted traction, in space and time, applied on a boundary of a 2D bounded solid. They utilized wave motion data from a limited number of sensors to estimate the traction profile. The study shows that the inversion performance without Tikhonov (TN) regularization is the same as the case with the regularization employed. To support the observation, the authors proved that their presented objective functional is quadratic—the relation from a force vector to wave responses is linear unlike the nonlinear material-wave relation—and convex. Guidio et al. [17] also studied a new approach for identifying the profile, in time and space, of an inclined wave which impinges a domain of SH wave motions. To mimic the incident wave, they applied traction on a truncated boundary.

Continuing the aforementioned works, herein, we introduce a novel procedure to (*i*) optimize dynamic body force on virtual interfaces such that it induces dynamic behaviors within a reduced domain to be consistent with observational data and, consequently, (*ii*) reconstruct targeted dynamic behaviors in a truncated domain. We also compare our optimized body force with the force at the same interfaces calculated by the DRM theory using targeted, unknown incident wave motions. The DRM was developed by Bielak et al. [18] and Yoshimura et al. [19], where incident waves are modeled as an effective seismic force along a DRM layer of finite elements. The DRM has been extensively employed to replicate seismic behaviors in truncated domains hit by an earthquake excitation, regardless of the location of a seismic hypocenter and the amplitudes, frequency contents, and incident angles of incoming waves. The DRM has been quite extensively utilized in various studies in earthquake engineering [20, 21, 22, 23, 24, 25, 26, 27, 28, 29, 30, 31, 32].

This paper presents numerical experiments that employ incoherently propagating incident waves and show that the reconstructed wave field accurately matches its targeted value. We report that our optimized force reconstructs the correct wave field in the interior area surrounded by the DRM interface. However, the optimized force can differ from the reference force computed by the standard DRM procedure. This is because we do not impose any constraint on the choice of solution among other possible solutions allowed by DRM. Fundamentally, as for any linear wave equations, DRM admits different decompositions of the incident and scattered waves of the same total wave field, where such property has been recently exploited in the context of analog computing [33]. In this paper, we developed a post-process procedure to modify an optimized force vector to find an alternative force vector such that the scattered wave field in the exterior domain is silenced.

2. Problem Definition

We consider a two-dimensional (2D) linear isotropic solid (Fig. 1(a)), truncated by wave-absorbing boundary conditions (WABC). The particle motion of the solid is considered to occur only in the anti-plane direction and to be attributed to shear-wave propagation. This study attempts to (i) optimize dynamic body forces at two virtual interfaces (i.e., Γ_b and Γ_e) in the solid and, then, (ii) replay the dynamic behaviors of the solid surrounded by WABC from surficial seismic measurements. The surficial measurements are attributed to wave motions in the domain that are induced by incident waves propagated from the outside of the domain.

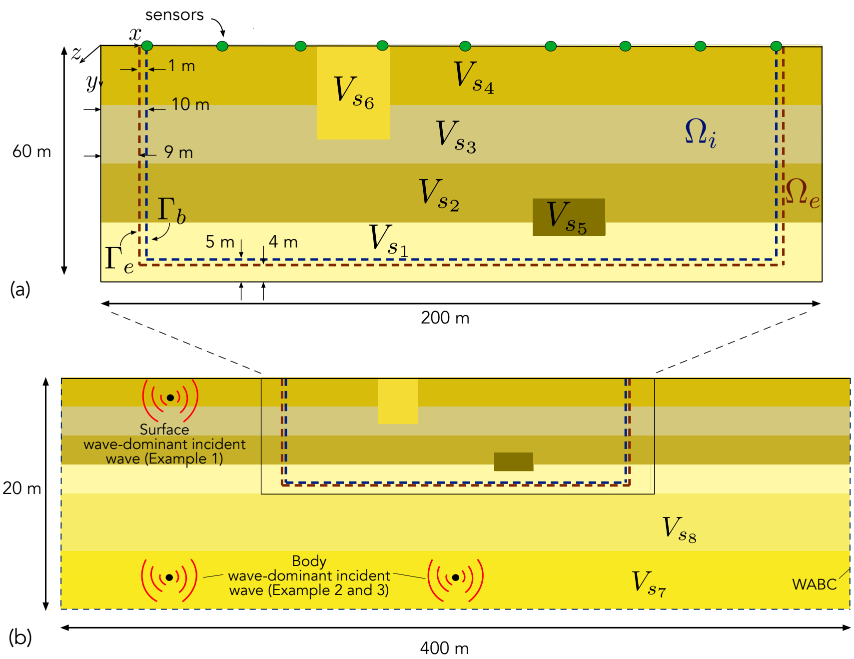

Figure 1: Enlarged domain used in the presented optimization problem. (a) a WABC-truncated domain is used for optimization of dynamic force at the virtual interfaces; (b) targeted dynamic behaviors are originally triggered by a seismic source outside the truncated solid, but the presented inversion solver is not informed of the source.

2.1. The governing equation

The governing differential equation of a shear wave in a 2D undamped solid domain for $(x, y) \in \Omega$ and $t \in J = (0, T]$ is defined as:

$$\nabla \cdot (G\nabla u) - \rho \frac{\partial^2 u}{\partial t^2} = 0, \quad \text{on } \Omega \times J, \tag{1}$$

where $u = u(x, y, t)$ represents the displacement field of wave motions in the z-plane, while the wave propagates in the x-y plane (i.e., SH wave motion); x and y are the horizontal and vertical coordinates. The medium is characterized by shear modulus $G(x, y)$ and mass density $\rho(x, y)$. The top surface (Γ_{top}) is subject to a traction-free condition:

$$\frac{\partial u}{\partial y}(x, 0, t) = 0, \qquad 0 \le x \le L, \tag{2}$$

while the WABC [34] are presented on the left (Γ_{left}), bottom (Γ_{bottom}), and right (Γ_{right}) boundaries:

$$\frac{\partial u}{\partial x} = -\frac{1}{V_s}\frac{\partial u}{\partial t}, \qquad x = 0, \quad D \le y \le 0, \tag{3}$$

$$\frac{\partial u}{\partial y} = -\frac{1}{V_s}\frac{\partial u}{\partial t}, \qquad 0 \le x \le L, \quad y = D, \tag{4}$$

$$\frac{\partial u}{\partial x} = -\frac{1}{V_s}\frac{\partial u}{\partial t}, \qquad x = L, \quad D \le y \le 0. \tag{5}$$

In the above, $V_s(x, y)$ denotes the shear wave velocity of the soil; D represents the y-coordinate of Γ_{bottom}; and L represents the x-coordinate of Γ_{right}. Lastly, the system is initially at rest:

$$u(x, y, 0) = 0, \quad \frac{\partial u}{\partial t}(x, y, 0) = 0. \tag{6}$$

2.2. Discrete state problem

We use the finite element method to solve the governing equation (1), where its semi-discrete equation reads:

$$\mathbf{M}\ddot{\mathbf{u}}(t) + \mathbf{C}\dot{\mathbf{u}}(t) + \mathbf{K}\mathbf{u}(t) = \mathbf{F}(t). \tag{7}$$

In the above, $\mathbf{u}(t)$ is a displacement solution vector at time t. $\mathbf{M}$, $\mathbf{C}$, and $\mathbf{K}$ are the global matrices, and $\mathbf{F}$ denotes the force vector. Our optimized force and effective seismic force (also dubbed a DRM force) on Γ_b and Γ_e will be defined in the force vector of the discrete form (i.e., the nodal forces along Γ_b and Γ_e). Please see Appendix A, which briefly describes how to compute DRM forces by using targeted incident (free-field) waves propagated from the outside of the truncated domain.

We solve the time-dependent equation (7) by using the implicit Newmark method, which allows us to formulate the forward wave simulation into the following compact form:

$$\mathbf{Q}\hat{\mathbf{u}} = \hat{\mathbf{F}}. \tag{8}$$

In the above, the matrix $\mathbf{Q}$ is the discrete forward operator comprised of the $\mathbf{M}$, $\mathbf{C}$, and $\mathbf{K}$ matrices of the semi-discrete equation and the Newmark time integrator [35] (the detail of $\mathbf{Q}$ can be seen in previous works [16, 17, 36], which used the $\mathbf{Q}$ matrix during the PDE-constrained optimization process). We use $\hat{\mathbf{u}}$ and $\hat{\mathbf{F}}$ to denote, respectively, the solution and global force vectors for all the time steps, i.e.,

$$\hat{\mathbf{u}} = \begin{bmatrix} \mathbf{u}_0 \\ \dot{\mathbf{u}}_0 \\ \ddot{\mathbf{u}}_0 \\ \vdots \\ \mathbf{u}_{\mathrm{N}} \\ \dot{\mathbf{u}}_{\mathrm{N}} \\ \ddot{\mathbf{u}}_{\mathrm{N}} \end{bmatrix}, \quad \hat{\mathbf{F}} = \begin{bmatrix} 0 \\ 0 \\ \mathbf{F}_0 \\ \vdots \\ \mathbf{F}_{\mathrm{N}} \\ 0 \\ 0 \end{bmatrix}, \tag{9}$$

where the subscript indicates the time step, and N represents the final time step.

3. Optimization Modeling

In this section, we describe the inverse problem for the optimized force vector $\hat{\mathbf{F}}^{\text{opt}}$ driven by the misfit between the measured and reconstructed wave motions at sensor locations on the surface. The discretize-then-optimize (DTO) method [16, 17, 36, 37] is utilized in the presented optimization modeling because of its relatively compact numerical procedure compared to the optimize-then-discretize (OTD) method. Using the optimized dynamic force at the virtual interfaces, we aim to reconstruct the wave motions in an interior domain truncated by WABC.

3.1. Control parameters

Under this optimization method, the control parameters ξ are determined as $P_{b_{kj}}$ and $P_{e_{kj}}$. They are components of $\hat{\mathbf{F}}^{\text{opt}}$ corresponding to γ_{b_k} and γ_{e_k}, respectively, and t_j. Here, γ_{b_k} is the k-th node on Γ_b, and γ_{e_k} is the k-th node on Γ_e; and t_j is the j-th time step. We note that γ_{b_k} and γ_{e_k} are numbered from the top-left discrete nodes of Γ_b and Γ_e to the top-right ones. Moreover, the components of $\hat{\mathbf{F}}^{\text{opt}}$, which are not part of the control parameters, are set to be zero.

3.2. Discrete Lagrangian functional

We are interested in finding the control parameters' values that result in a minimum of a discrete objective functional:

$$\hat{\mathcal{L}} = \frac{1}{2}(\hat{\mathbf{u}} - \hat{\mathbf{u}}_{\text{m}})^T \,\overline{\mathbf{B}}\, (\hat{\mathbf{u}} - \hat{\mathbf{u}}_{\text{m}}), \tag{10}$$

where $\hat{\mathbf{u}}$ corresponds to the discretization, in space and time, of $u(x, y, t)$ induced by a set of optimized $P_{b_{kj}}$ and $P_{e_{kj}}$; $\hat{\mathbf{u}}_{\text{m}}$ is the discretization, in space and time, of $u_{\text{m}}(x, y, t)$, which is the targeted wave response induced by incident seismic waves propagated from the outside of the truncated domain. In (10), $\overline{\mathbf{B}}$ represents $\Delta t\mathbf{B}$, where $\mathbf{B}$ is a square matrix with mostly zeros except for few diagonal components correspond to sparsely-distributed sensors. We synthetically generate $\hat{\mathbf{u}}_{\text{m}}$ by using our FEM solver with an enlarged domain, where a point seismic source induces the wave motions (see Fig. 1(b)).

In addition to the objective functional, the discrete state problem (8) is imposed as a side constraint to $\hat{\mathcal{L}}$ via the use of a Lagrange multiplier vector $\hat{\lambda}$. There results in the following Lagrangian functional $\hat{\mathcal{A}}$:

$$\hat{\mathcal{A}} = \frac{1}{2}(\hat{\mathbf{u}} - \hat{\mathbf{u}}_{\text{m}})^T \,\overline{\mathbf{B}}\, (\hat{\mathbf{u}} - \hat{\mathbf{u}}_{\text{m}}) - \hat{\lambda}^T(\mathbf{Q}\hat{\mathbf{u}} - \hat{\mathbf{F}}^{\text{opt}}), \tag{11}$$

where

$$\hat{\lambda} = \left[\lambda_0^T, \dot{\lambda}_0^T, \ddot{\lambda}_0^T, .., \lambda_{\text{N}}^T, \dot{\lambda}_{\text{N}}^T, \ddot{\lambda}_{\text{N}}^T,\right]^T. \tag{12}$$

3.3. The three first-order optimality conditions

We optimize the control parameters by satisfying the three first-order optimality conditions. In the first condition, the derivative of $\hat{\mathcal{A}}$ with respect to $\hat{\lambda}$ vanishes when we solve the state equation (8) by using $\hat{\mathbf{F}}^{\text{opt}}$:

$$\frac{\partial \hat{\mathcal{A}}}{\partial \hat{\lambda}} = -\mathbf{Q}\hat{\mathbf{u}} + \hat{\mathbf{F}}^{\text{opt}} = 0. \tag{13}$$

Next, the second condition, the vanishing derivative of $\hat{\mathcal{A}}$ with respect to $\hat{\mathbf{u}}$, leads us to the adjoint equation:

$$\frac{\partial \hat{\mathcal{A}}}{\partial \hat{\mathbf{u}}} = \underbrace{-\mathbf{Q}^T \hat{\lambda} + \overline{\mathbf{B}}\, (\hat{\mathbf{u}} - \hat{\mathbf{u}}_{\text{m}}) = 0}_{\text{adjoint problem}}. \tag{14}$$

We note that the adjoint problem is a final-value problem, as opposed to the original initial-value state problem, which is identified by $\mathbf{Q}^T \hat{\lambda}$ term in (14). The adjoint method (14) can be solved by marching backward in time as shown in our previous work [17].

The third condition makes the derivative of $\hat{\mathcal{A}}$ with respect to $\hat{\mathbf{F}}^{\text{opt}}$ to vanish and yields the next control equation:

$$\frac{\partial \hat{\mathcal{A}}}{\partial \hat{\mathbf{F}}^{\text{opt}}} = \hat{\lambda} = 0, \tag{15}$$

which indicates that $\frac{\partial \hat{\mathcal{A}}}{\partial \hat{\mathbf{F}}^{\text{opt}}} = \frac{\partial \hat{\mathcal{L}}}{\partial \hat{\mathbf{F}}^{\text{opt}}}$ is a vector of the components of $\hat{\lambda}$ corresponding to the discrete node numbering and the time step of $\boldsymbol{\xi}$. Eq. (15) is satisfied at an optimal value of control parameters, where both the objective functional and the source term of the adjoint problem (14) vanish.

4. Numerical Implementation

The algorithm iteratively optimizes the control parameters using the gradient-based minimization method by employing the semi-analytically evaluated gradient vector $\nabla_{\boldsymbol{\xi}} \hat{\mathcal{L}}$ as follows:

(a) First, $\hat{\mathbf{u}}_{\mathrm{m}}$ are synthetically generated by considering incident seismic waves. Namely, we compute the wave solutions in an enlarged domain, which contains a point seismic source.

(b) An optimized $\hat{\mathbf{F}}^{\mathrm{opt}}$, comprised of control parameters $\boldsymbol{\xi}$ (all zero-valued at the initial iteration), is utilized to obtain $\hat{\mathbf{u}}$ by solving the state problem.

(c) Next, $\hat{\lambda}$ is computed by solving the adjoint equation using $\hat{\mathbf{u}}$ and $\hat{\mathbf{u}}_{\mathrm{m}}$.

(d) The gradient of the objective functional, $\nabla_{\boldsymbol{\xi}} \hat{\mathcal{L}}$, is calculated by using the adjoint solution.

(e) We use the conjugate-gradient method to find the best search direction, $\mathbf{d}$, where an optimal step length, h, is calculated by using the Newton's method [16].

(f) Lastly, the gradient-based scheme refreshes the approximate $\boldsymbol{\xi}$ using the search direction and optimal step length as: $\boldsymbol{\xi}_{\text{updated}} = \boldsymbol{\xi}_{\text{previous}} + \mathbf{d}\, h$.

The above procedures, (b) to (f), are consistently repeated by the optimizer, which searches to determine the control parameters that make the control equation to vanish as (15). We discontinue the iteration of the optimizer either when the $\hat{\mathcal{L}}_{\text{updated}}$ is smaller than $\hat{\mathcal{L}}_{\text{initial}} \times 10^{-7}$ or when the iteration number is greater than 1000.

5. Numerical Results

We conduct numerical experiments to study the performance of the outlined optimization procedure for updating $\hat{\mathbf{F}}^{\mathrm{opt}}$ at the virtual interface boundaries (Γ_b and Γ_e) and eventually reconstructing the wave responses—induced by incident seismic waves propagated from the outside of the truncated domain—in Ω_i delineated by the DRM boundary in a near-surface area with respect to various factors.

The proposed objective functional is driven only by the measurements of the sparsely distributed sensors on the surface without information on the choice of scattered field in the exterior domain. Thus, we expect that the optimized force $\hat{\mathbf{F}}^{\mathrm{opt}}$ may differ from the reference force $\hat{\mathbf{F}}^{\mathrm{eff}}$ constructed by the standard DRM procedure. However, $\hat{\mathbf{F}}^{\mathrm{opt}}$ is a valid solution; thus, it is unnecessary to obtain the same reference force, i.e., the standard DRM force. Instead, an alternative effective seismic force that gives a silent scattered field may serve as another reference force. Thus, we introduce a post-process procedure to modify the optimized force to achieve a zero scattering field in the exterior domain and compare it with the alternative effective seismic force.

For all examples, we reconstruct the ground motions in Ω_i of a 4-layered solid with 2 inclusions, as shown in Fig. 1(a). The truncated domain is set to be 200 m × 60 m with shear wave speeds V_{s_1} to V_{s_6} of 300, 250, 200, 150, 800, and 1000 m/s. We also consider that a mass density (ρ) is uniform as 1500 kg/m^3 in the entire domain. We placed sensors in a manner such that the first sensor is always placed in the top-left corner of Γ_b, and the last one is located in the top-right corner of Γ_b. The truncated domain is a subset of the enlarged domain, as shown in Fig. 1(b). The enlarged domain is employed to obtain targeted wave response $\hat{\mathbf{u}}_{\mathrm{m}}$, of which surficial measurements are used in our optimization procedure per (10). Its dimension is 400 m × 120 m, and the wave speeds at the lower part of the enlarged domain are set to be $V_{s_7} = 1800$ m/s and $V_{s_8} = 1500$ m/s, respectively.

The presented method requires that the inversion simulator is informed of the spatial distribution of wave speeds in a reduced domain, which can be obtained via a prior site characterization technique (e.g., spectral analysis of surface waves (SASW) method [38, 39, 40, 41, 42], multi-channel analysis of surface waves (MASW) method [43, 44], or full-waveform inversion (FWI) [12, 13, 45]. The truncated, reduced model is the domain of interest, where we intend to reconstruct its response to a seismic activity, and the domain contains the surface on which we sparsely measure the response. The dimension of the enlarged domain is chosen to generate synthetic data that are originally attributed to a source located outside of the domain of interest. Thus, we determined the dimensions of the reduced and the enlarged domains in a manner such that the enlarged domain must contain the reduced model and be sufficiently large to include a seismic source. As long as this condition is met, the presented method can be generalized for any dimensions of reduced and enlarged domains that a computing resource can permit. Namely, the method is not limited to the presented dimensions of 200 by 60 m and 400 by 120 m.

We use an error norm to quantify the difference of the reconstructed ground motions at interior nodes $\mathbf{u}_j^{\text{interior}}$ from their targeted counterpart $\mathbf{u}_{\text{m}_j}^{\text{interior}}$ at all the time steps for t_j, which reads:

$$\mathcal{E}^u = \sum_{j=1}^{N} \frac{|\mathbf{u}_{\text{m}_j}^{\text{interior}} - \mathbf{u}_j^{\text{interior}}|^2}{|\mathbf{u}_{\text{m}_j}^{\text{interior}}|^2} \times 100[\%]. \tag{16}$$

The difference between the optimized force $\hat{\mathbf{F}}^{\text{opt}}$ to its reference value $\hat{\mathbf{F}}^{\text{eff}}$ is measured by:

$$\mathcal{E} = \frac{|\hat{\mathbf{F}}^{\text{eff}} - \hat{\mathbf{F}}^{\text{opt}}|^2}{|\hat{\mathbf{F}}^{\text{eff}}|^2} \times 100[\%]. \tag{17}$$

We analyze the effectiveness of the proposed optimization method with respect to the frequency content of the incident wave, the number of sensors utilized on the top surface, and an incident angle in which the incident seismic waves are propagated from the outside of the truncated domain. The presented optimizer is tested by incident waves, that do not mimic plane waves but those in realistic seismic activity, as shown in Examples 1 to 3. Example 4 investigates the performance of the optimizer for a plane incoming wave of a dominant incident angle.

For all numerical examples, the spatial and temporal intervals for the discretization of $\hat{\mathbf{F}}^{\text{opt}}$ and $\hat{\mathbf{u}}$ are 1 m and 0.001 s, respectively.

5.1. Example 1: Assessing the performance to reconstruct ground motions induced by surface wave-dominant incident waves

We evaluate the performance of optimizing the dynamic force at the virtual interfaces and reconstructing the dynamic behaviors in Ω_i in a case where dynamic behaviors are attributed to surface wave-dominant incident waves impinging the reduced domain.

To this end, we generate the incident waves in the enlarged domain, which encompasses a point wave source at x = -40 m and y = 10 m with its force time signal being a Ricker wavelet signal:

$$f(x, y, t) = -100 \times \frac{(0.25\eta^2 - 0.5)e^{-0.25\eta^2} - 13e^{-13.5}}{0.5 + 13e^{-13.5}}, \qquad t \leq \bar{t}, \tag{18}$$

where $\eta = \omega t - 3\sqrt{6}$; $\bar{t} = 6\sqrt{6}/\omega$; $\omega = 2\pi f_c$; and f_c is the central frequency of the signal. We note that Ricker pulses are used to characterize a seismic source with a continuous spectrum, and by setting their f_c to be less than 10 Hz, we aim to mimic the frequency spectrum of typical seismic activity. Fig. 2 shows the time histories of Ricker signals of dominant frequencies of 2, 5, and 10 Hz, and the frequency content of each signal.

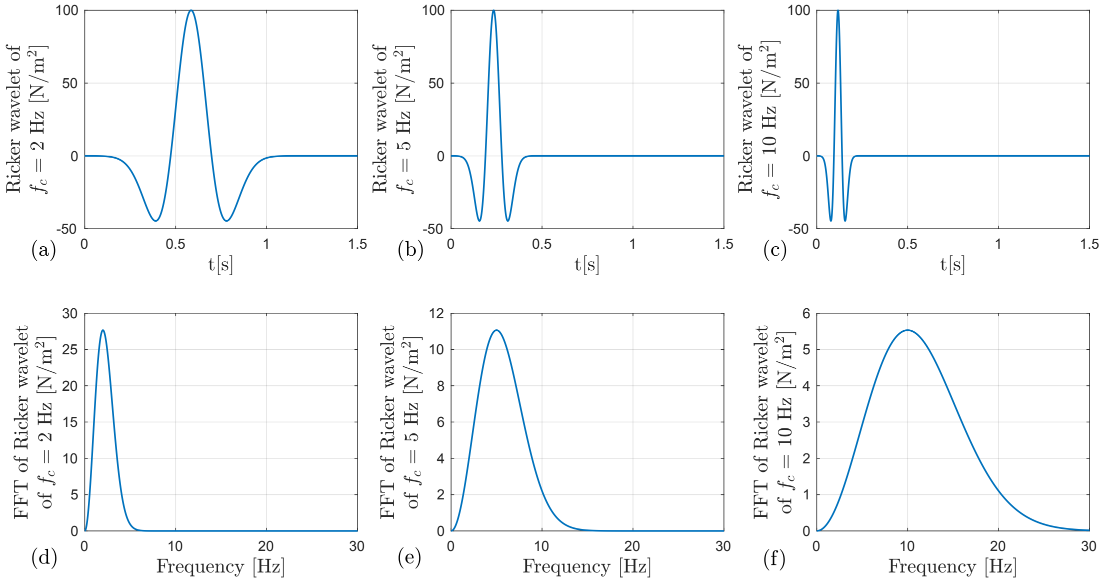

Figure 2: (a-c) Time histories and (d-f) frequency content of Ricker wavelet signals of central frequencies of 2, 5, and 10 Hz, respectively.

5.1.1. *Optimization without post-processing*

Fig. 3 presents how $\mathcal{E}^u$ depends on the dominant frequency of the point source that generates incident waves and the sensor spacing in Example 1. Fig. 3 presents that, when we use a sensor spacing of up to 5 m, i.e., 37 sensors on the surface, the optimization solver accurately estimates the wave responses in Ω_i ($\mathcal{E}^u \leq 2\%$) for surface wave-like waves of their dominant frequencies of 2, 5, and 10 Hz. For the spacing of the sensors of 10 m, the solver cannot reconstruct the dynamic behaviors in Ω_i for the dominant frequency of 10 Hz ($\mathcal{E}^u = 14.6\%$) as accurately as 5 Hz ($\mathcal{E}^u = 2\%$) and 2 Hz ($\mathcal{E}^u = 1\%$). Overall, the desired sensor spacing decreases as the dominant frequency of the surface-dominant incident wave increases.

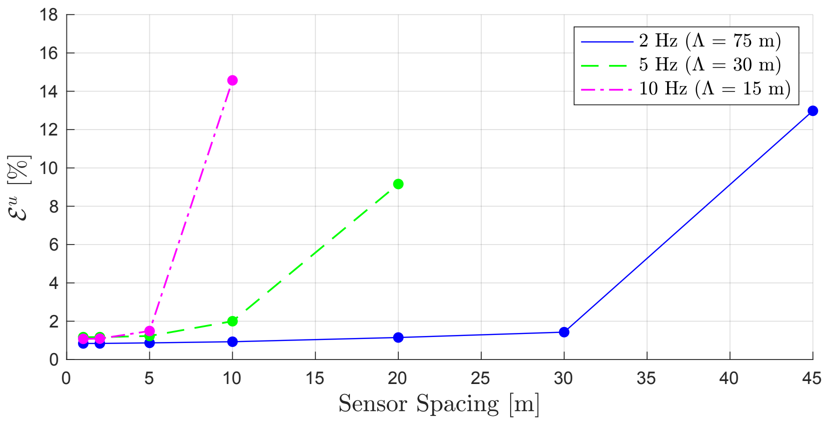

Figure 3: Example 1 - Relation of the reconstruction accuracy to the dominant frequency (or wavelength Λ) of the surface wave-dominant incident waves and the sensor spacing.

Fig. 4(a) shows the targeted dynamic responses in Ω_i that are computed from the enlarged domain solver, and Fig. 4(b) to (d) show their reconstructed counterparts for a different value of sensor spacing, when a 10 Hz Ricker source signal is used in the enlarged domain simulator. The time steps (t) shown in Fig. 4 (0.6 s, 0.8 s, and 1.0 s) are based on the time elapsed since the source's Ricker signal is initiated. We note, from Fig. 4, that, as the spacing of the sensors is increased, the agreement between the targeted and reconstructed motions in Ω_i diminishes.

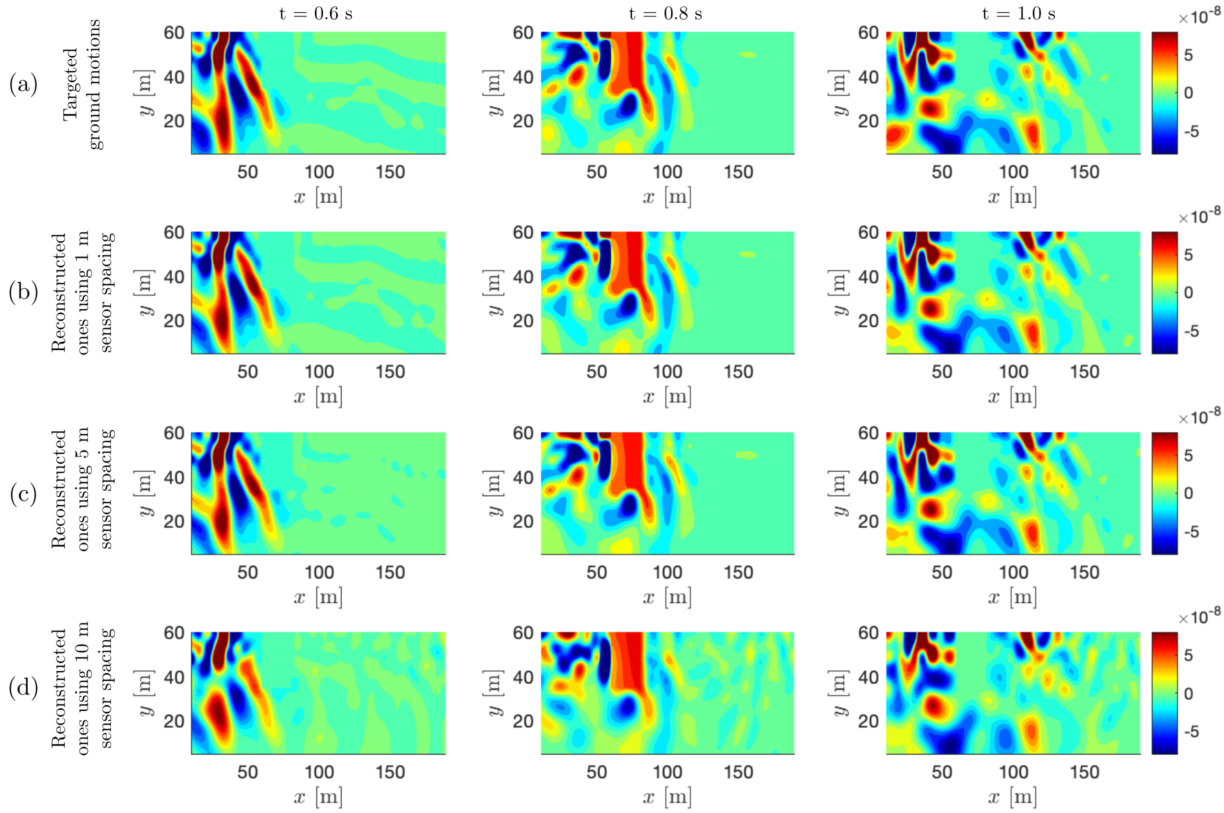

Figure 4: Example 1 - (a) Targeted dynamic motions in Ω_i caused by surface wave-like incoming waves of an dominant frequency 10 Hz and (b-d) reconstructed motions for different sensor spacing (1, 5, and 10 m).

Fig. 5 shows the excellent agreement between the measured data u_{m} obtained by using the enlarged domain, and their reconstructed counterparts u induced by $\hat{\mathbf{F}}^{\mathrm{opt}}$ at nineteen different locations on Γ_{top} when we utilize the 10 Hz Ricker source signal and the sensor spacing of 1 m.

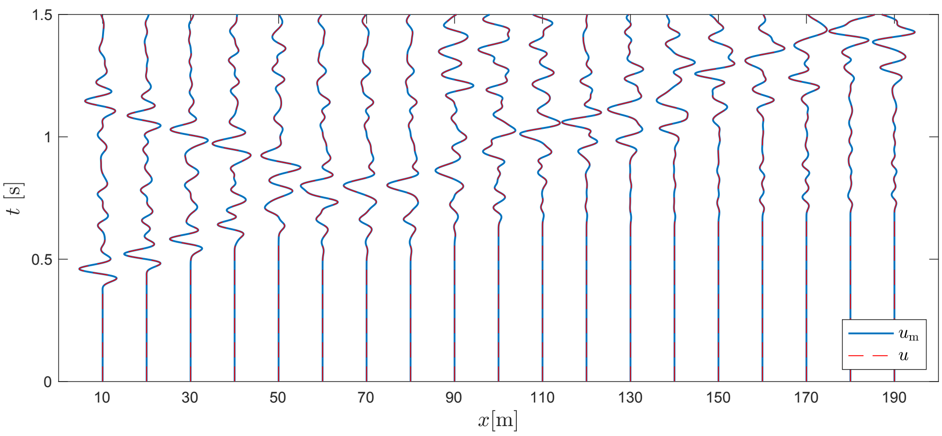

Figure 5: Example 1 - Comparison between the measured data u_{m} and the computed signals u induced by $\hat{\mathbf{F}}^{\mathrm{opt}}$ at 19 different locations on Γ_{top}.

In Fig. 6, we examine the amplitudes of the scattered waves in the exterior domain induced by $\hat{\mathbf{F}}^{\mathrm{opt}}$ and $\hat{\mathbf{F}}^{\mathrm{eff}}$, which is built by the free-field incident waves propagated from the outside of the truncated domain. The sensor spacing is 1 m, and the 10 Hz Ricker source signal is utilized. The optimized force $\hat{\mathbf{F}}^{\mathrm{opt}}$ induces relatively large amplitudes in the exterior domain Ω_e, the outer region of the dashed line, compared to the scattered wave in Ω_e induced by $\hat{\mathbf{F}}^{\text{eff}}$. This difference implies that there is more than one choice of incident-scatttered wave decompositions for an identical total wave. Namely, a total wave $\mathbf{u}^{\text{t}}$ can be decomposed into an incident wave $\mathbf{u}^0$ and a scattered wave $\mathbf{u}^{\text{s}}$ as the following:

$$\mathbf{u}^{\text{t}} = \mathbf{u}^0 + \mathbf{u}^{\text{s}}. \tag{19}$$

In the above, $\mathbf{u}^{\text{s}}$ is defined as a scattered wave from local features in an interior domain impinged by $\mathbf{u}^0$ per the standard DRM. However, we can also define $\mathbf{u}^{\text{s}}$ in a manner such that $\mathbf{u}^0$ is identical to $\mathbf{u}^{\text{t}}$, and $\mathbf{u}^{\text{s}}$ is silenced. With such a modified free-field, the new decomposition leads to a modified effective seismic force as an alternative.

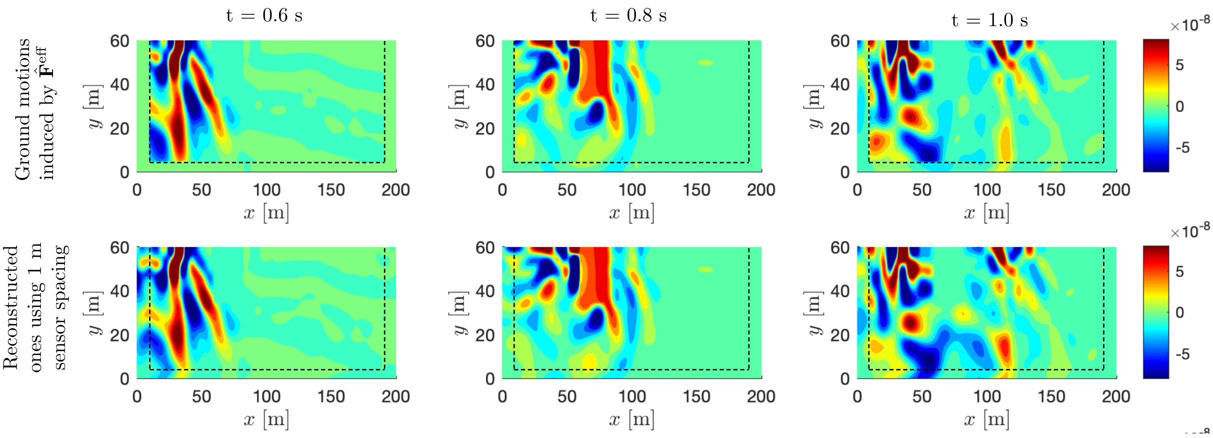

Figure 6: Example 1 - Ground motions in the domain induced by the effective force and the optimized force using 1 m sensor spacing; and the scattered waves of reference ground motions and reconstructed ground motions, for the case that considers a Ricker pulse signal of 10 Hz. The dashed line indicates a DRM boundary Γ_b.

Figs. 7 and 8 highlight the difference between the optimized dynamic force vector $\hat{\mathbf{F}}^{\text{opt}}$ and $\hat{\mathbf{F}}^{\text{eff}}$, where the error is quantified as $\mathcal{E} = 97.43\%$. Specifically, Fig. 8 shows the effective and optimized control parameters corresponding to the nodes on Γ_e and Γ_b at $x = 9$ m and 10 m, respectively, and $y = 10$ m and for every time step. In the following section, we discuss this seemingly different behavior in detail and introduce post-processing to alter the optimized force, which will be compared with the modified effective seismic force.

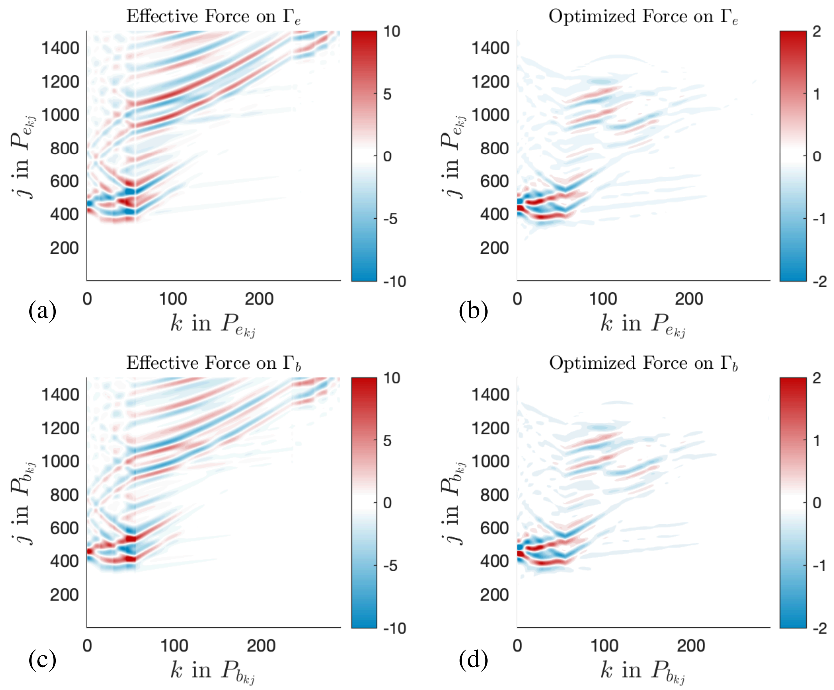

Figure 7: Example 1 - (a) Effective seismic force and (b) its final-optimized counterpart on Γ_e, and (c) effective seismic force and (d) its final-optimized counterpart on Γ_b when a Ricker of 10 Hz as the seismic source signal and a sensor spacing of 1 m are used.

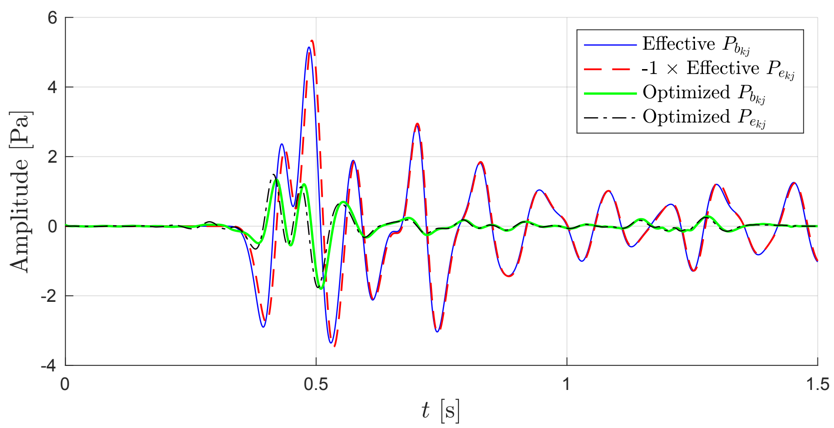

Figure 8: Example 1 - Time signals of effective and optimized forces at x = 9 m and 10 m (Γ_e and Γ_b, respectively) and y = 10 m when a Ricker of 10 Hz and a sensor spacing of 1 m are used.

5.1.2. Post-processing the optimized force

In the standard DRM procedure, shown in Appendix Appendix A, an effective force vector $\hat{\mathbf{F}}^{\text{eff}}$ is obtained from free-field ground motions ($\mathbf{u}^0$ and $\ddot{\mathbf{u}}^0$ on Γ_b and in Ω_e), which are computed in an enlarged domain without considering the wave speeds of local features, such as the inclusions of V_{s_5} and V_{s_6} in Fig. 1. Thus, when simulated with the effective force, the scattered field in the exterior domain exclusively reveals the effect of the local features.

Alternatively, we introduce a modified effective force vector $\hat{\mathbf{F}}^{\text{eff}}_{\text{mod}}$ by using the "modified" free-field ground motions ($\mathbf{u}^{0_{\text{mod}}}$ and $\ddot{\mathbf{u}}^{0_{\text{mod}}}$ on Γ_b and in Ω_e), which are computed in an enlarged domain taking into account the local features (Appendix Appendix B). The modified effective force $\hat{\mathbf{F}}^{\text{eff}}_{\text{mod}}$ differs from the original effective force vector $\hat{\mathbf{F}}^{\text{eff}}$ in a manner such that $\hat{\mathbf{F}}^{\text{eff}}_{\text{mod}}$ leads to zero scattered field in Ω_e. In the following, we modify both reference and optimized force vectors to provide a direct comparison.

We refer the modification on the optimized force vector as post-processing, which reads:

$$\hat{\mathbf{F}}_{\text{pp}}^{\text{opt}} = \mathbf{Q}\,\hat{\mathbf{u}}_{\text{pp}}. \tag{20}$$

In the above, $\hat{\mathbf{u}}_{\text{pp}}$ is rebuilt from $\hat{\mathbf{u}}$ by making the components of $\hat{\mathbf{u}}$ corresponding to Ω_e to vanish. Namely,

$$\hat{\mathbf{u}}_{\text{pp}} = \mathbf{D}\,\hat{\mathbf{u}}, \tag{21}$$

where $\mathbf{D}$ is a square, diagonal matrix, of which component is one everywhere except on the zero-valued diagonal components corresponding to nodes on Ω_e.

Fig. 9 shows that the modified effective force $\hat{\mathbf{F}}_{\text{mod}}^{\text{eff}}$ are in agreement with its post-processed optimized counterpart $\hat{\mathbf{F}}_{\text{pp}}^{\text{opt}}$: the error $\mathcal{E}$ between them is 15.21%, which is a lot smaller than $\mathcal{E} = 97.43\%$ between $\hat{\mathbf{F}}^{\text{eff}}$ and $\hat{\mathbf{F}}^{\text{opt}}$. Particularly, as far as the forces only at the upper-left portion of Γ_e and Γ_b at x of 9 and 10 m, respectively, and 0 m $\leq y \leq$ 30 m (i.e., $1 \leq k$ in $P_{kj} \leq 31$) are concerned, the error $\mathcal{E}$ is only 1.45%. It is because, for this surface-wave dominant incident wave, the wave response that is induced by $\hat{\mathbf{F}}_{\text{pp}}^{\text{opt}}$ at the upper-left portion on the virtual interfaces accounts for the surficial measurement data more significantly than its counterpart that is induced by $\hat{\mathbf{F}}_{\text{pp}}^{\text{opt}}$ at the other part of the virtual interfaces. Therefore, the measurement data drive our optimizer in a manner such that the part of $\hat{\mathbf{F}}_{\text{pp}}^{\text{opt}}$ at the upper-left portion of Γ_e and Γ_b matches $\hat{\mathbf{F}}_{\text{mod}}^{\text{eff}}$ better than the other part of $\hat{\mathbf{F}}_{\text{pp}}^{\text{opt}}$. Fig. 10 shows the agreement between modified effective forces and their post-processed optimized counterparts corresponding to the nodes on the upper-left portion of Γ_e and Γ_b at x of 9 and 10 m, respectively, and y of 10 m.

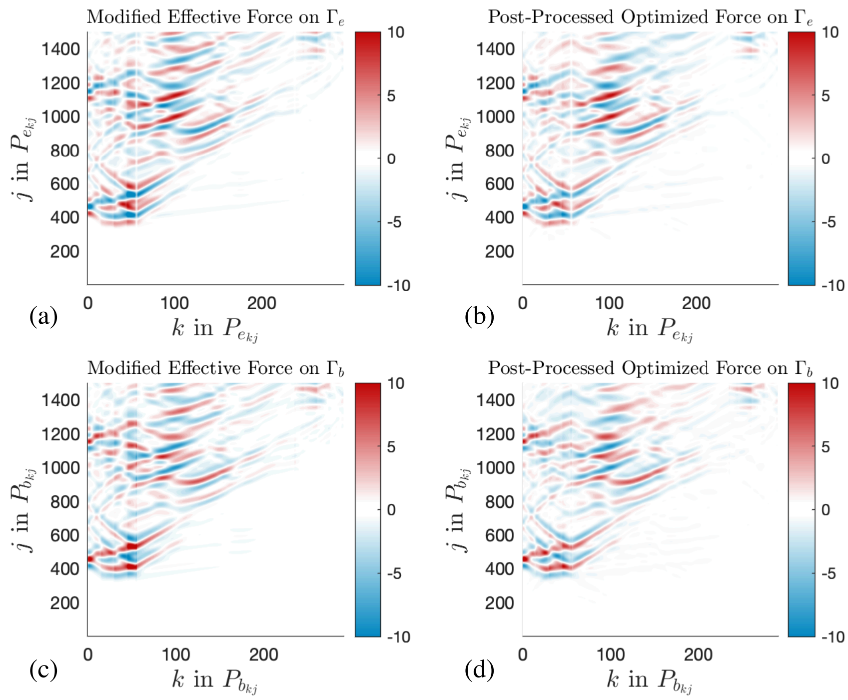

Figure 9: Example 1 - (a) Modified effective seismic force and (b) its post-processed optimized counterpart on Γ_e, and (c) modified effective seismic force and (d) its post-processed optimized counterpart on Γ_b when a Ricker of 10 Hz as the seismic source signal and a sensor spacing of 1 m are used.

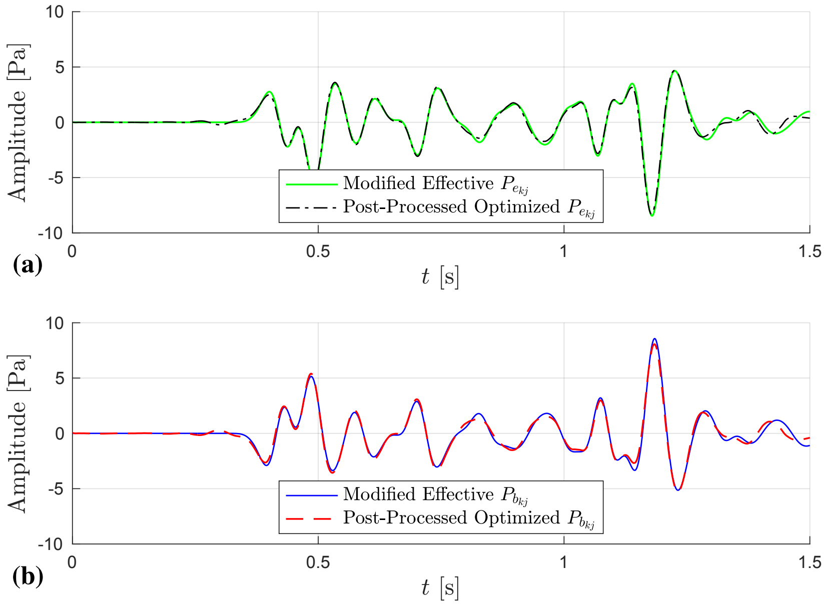

Figure 10: Example 1 - Time signals of modified effective and post-processed optimized forces at (a) x = 9 m and y = 10 m on Γ_e, and (b) x = 10 m and y = 10 m on Γ_b, when a Ricker of 10 Hz and a sensor spacing of 1 m are used.

5.2. Example 2: Studying the accuracy to reconstruct dynamic responses caused by body wave-dominant, oblique incoming waves

This example focuses on evaluating the performance of the proposed optimization algorithm for identifying dynamic responses in Ω_i caused by incoherently-propagating body-wave-dominant, oblique incoming waves. The same enlarged domain used in the previous example is used for generating the incident waves. We use a Ricker source in the bottom-left area of the enlarged domain, at x = -40 m and y = 100 m, in this example to obtain the synthetic measurement data. We note that the incident waves propagate as inclined waves in the reduced domain of interest.

In Fig. 11, we present the targeted and reconstructed dynamic motions in Ω_i for the 10 Hz Ricker source in the enlarged domain. As the spacing of sensors increases, the mismatch between the targeted and reconstructed dynamic responses in Ω_i grows, as shown in Fig. 11. Fig. 12 also shows the desired sensor spacing required to effectively estimate dynamic responses in Ω_i. A denser array of sensors is required to effectively estimate higher-frequency dynamic responses.

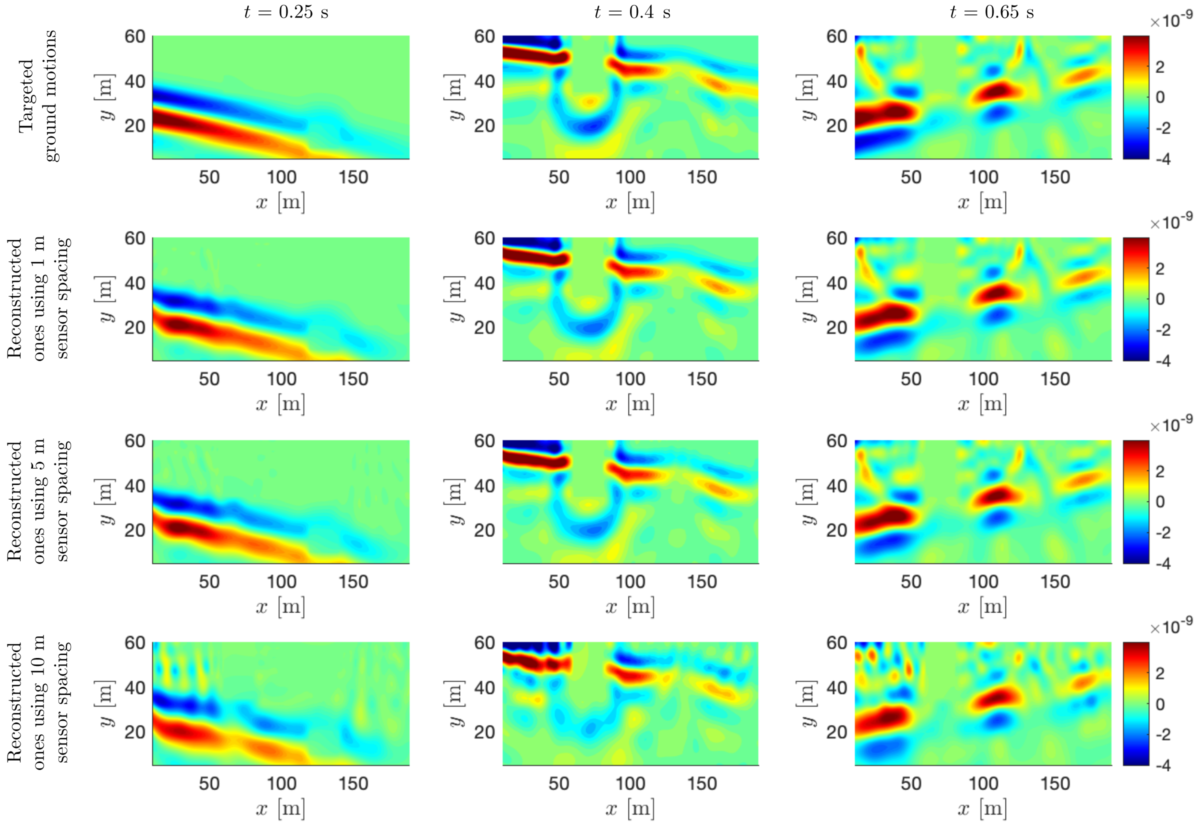

Figure 11: Example 2 - Targeted dynamic motions in Ω_i caused by incoming waves from a source in the bottom-left corner of the enlarged domain with a dominant frequency 10 Hz and reconstructed motions for different sensor spacing (1, 5, and 10 m).

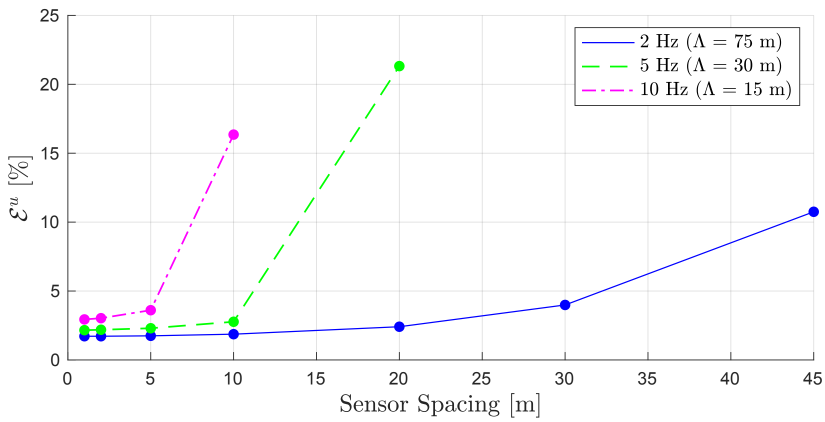

Figure 12: Example 2 - Relation of the reconstruction accuracy to the dominant frequency (or wavelength Λ) of a body wave-dominant incident wave and the sensor spacing.

Figs. 13 and 14 compare reference and optimized force vectors and their modified/post-processed versions. The error between the modified/post-processed vectors is $\mathcal{E} = 13.01\%$. The error reduces to 1.19% when considering the forces only at the bottom-center portion of Γ_b and Γ_e at 85 m $\leq x \leq$ 115 m and y of 55 and 56 m, respectively (i.e., $131 \leq k$ in $P_{b_{kj}} \leq 161$ and $133 \leq k$ in $P_{e_{kj}} \leq 163$). Fig. 15 shows the agreement between modified effective control parameters and their post-processed optimized counterparts corresponding to the nodes on the bottom-center portion

265 of Γ_e and Γ_b at x of 100 m and y of 56 and 55 m, respectively.

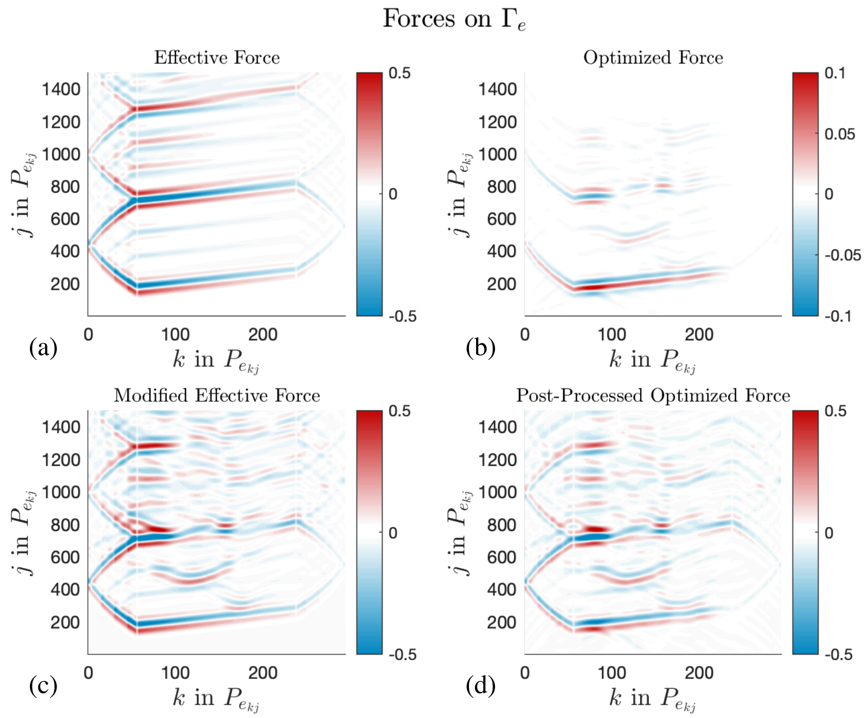

Figure 13: Example 2 - (a) Effective seismic force and (b) its final-optimized counterpart; and (c) modified effective seismic force and (d) its post-processed optimized counterpart on Γ_e when a Ricker of 10 Hz and a sensor spacing of 1 m are used.

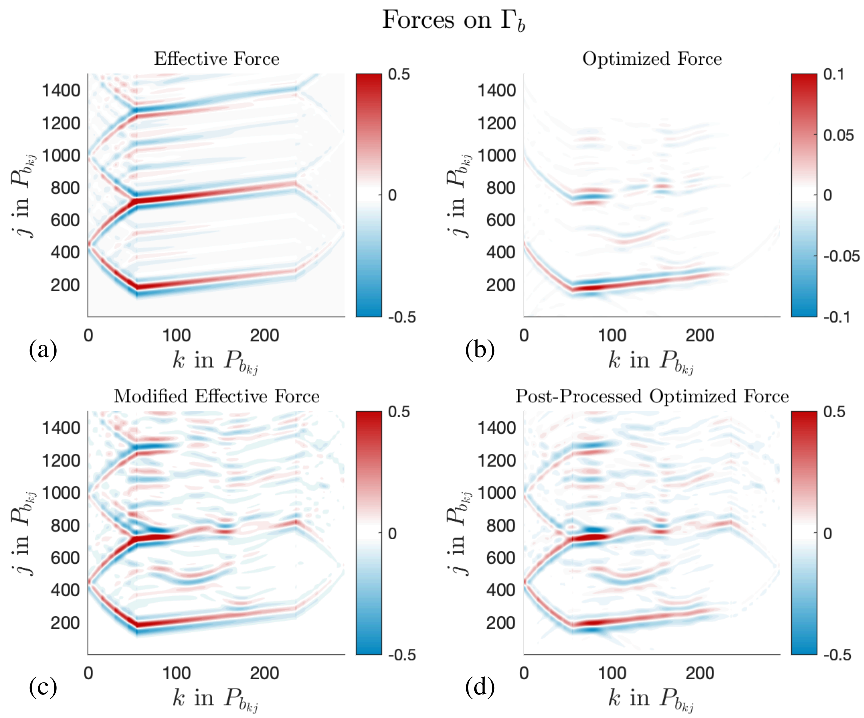

Figure 14: Example 2 - (a) Effective seismic force and (b) its final-optimized counterpart; and (c) modified effective seismic force and (d) its post-processed optimized counterpart on Γ_b when a Ricker of 10 Hz and a sensor spacing of 1 m are used.

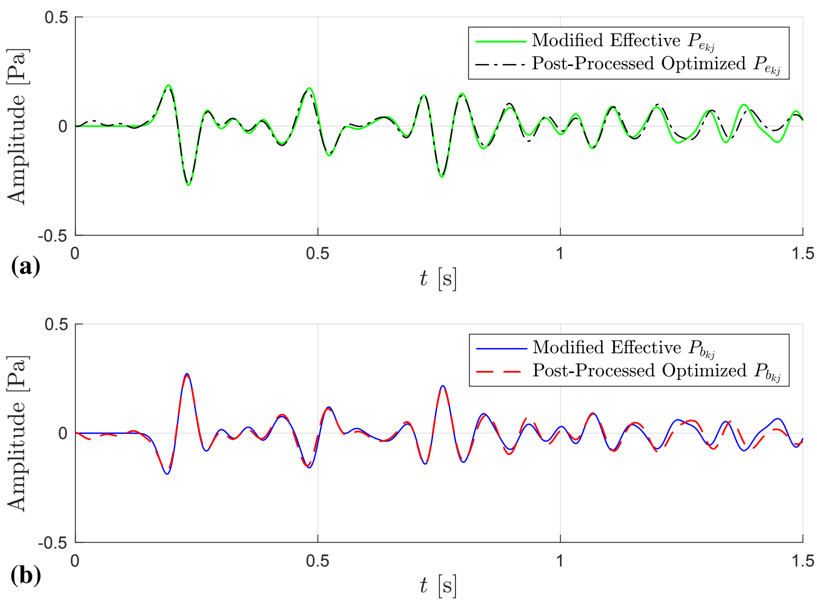

Figure 15: Example 2 - Time signals of modified effective and post-processed optimized forces at (a) x = 100 m and y = 56 m on Γ_e, and (b) x = 100 m and y = 55 m on Γ_b, when a Ricker of 10 Hz and a sensor spacing of 1 m are used.

5.3. *Example 3: Examining the numerical performance to reconstruct ground motions induced by body wave-dominant, arc-shaped incident waves*

Here, we consider a seismic source in the bottom-center part (at x = 100 m and y = 100 m) of the same enlarged domain. The resulted incident wave propagates as an arc-shaped wave in the reduced domain of interest.

Fig. 16 shows the targeted dynamic motions in Ω_i, which are initiated by the arc-shaped body wave-dominant incident wave in the enlarged domain, and their estimated counterparts in the case where incident waves are characterized by a 10 Hz Ricker source signal. As the sensor spacing increases, we notice a reduction in the effectiveness to estimate the dynamic responses in Ω_i. Thus, this example, again, serves as another example illustrating that our optimization simulator can successfully estimate body wave-dominant dynamic responses in Ω_i if the sensor spacing is small enough for a given frequency of an incident wave.

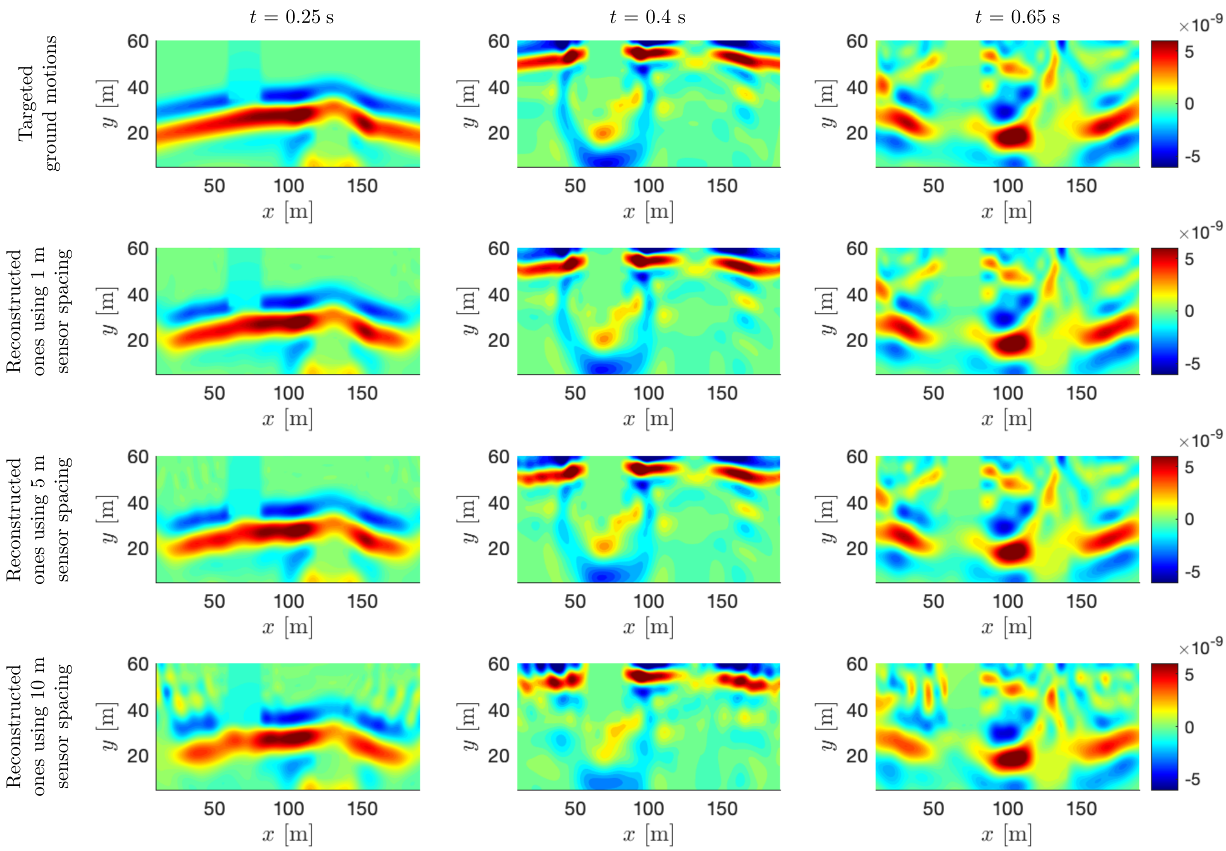

Figure 16: Example 3 - Targeted dynamic motions in Ω_i caused by arc-shaped incoming waves from a source in the bottom center of the enlarged domain with a dominant frequency 10 Hz and reconstructed motions for different sensor spacing (1, 5, and 10 m).

Fig. 17 shows that the frequency content of the incident wave and the sensor spacing are related to the performance of reconstructing wave responses in Ω_i as mentioned in previous examples.

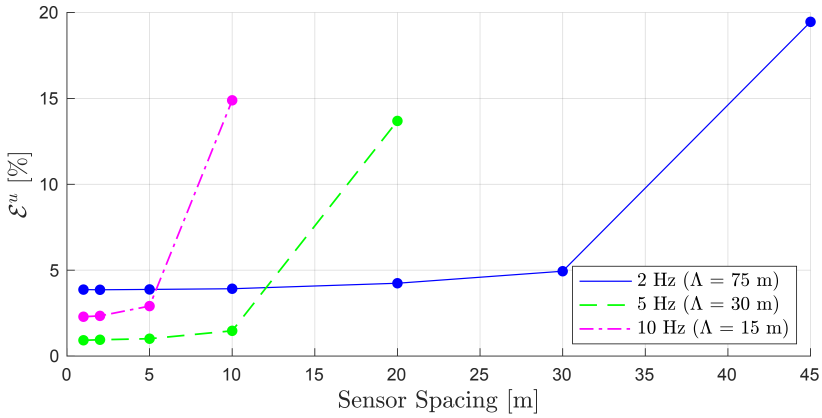

Figure 17: Example 3 - Relation of the reconstruction accuracy to the dominant frequency (or wavelength Λ) of a body wave-dominant arc-shaped incident waves and the sensor spacing.

The optimized force vector is compared with its reference value in Figs. 18 and 19. We observed that the post-processed optimized force vector exhibits a small error of $\mathcal{E} = 8.23\%$ when it is compared with the modified effective force. The error at the bottom-center portion of Γ_b and Γ_e at 85 m $\leq x \leq$ 115 m and y of 55 and 56 m, respectively (i.e., $131 \leq k$ in $P_{b_{kj}} \leq 161$ and $133 \leq k$ in $P_{e_{kj}} \leq 163$) decreases to 1.43%. Furthermore, Fig. 20 highlights the excellent agreement between modified effective control parameters and their post-processed optimized counterparts at nodes on the bottom-center portion of Γ_e and Γ_b at x of 100 m and y of 56 and 55 m, respectively.

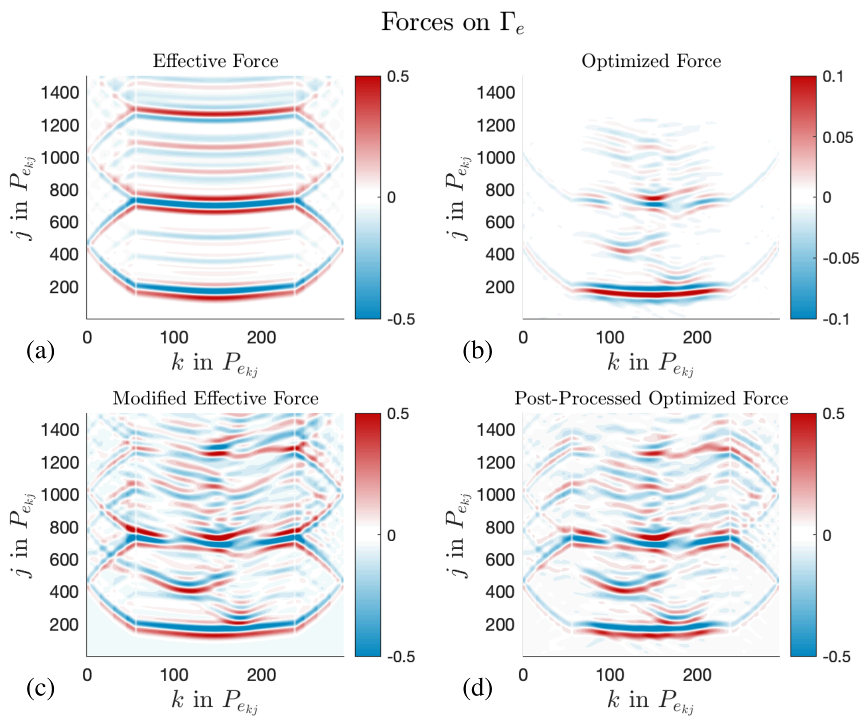

Figure 18: Example 3 - (a) Effective seismic force and (b) its final-optimized counterpart; and (c) modified effective seismic force and (d) its post-processed optimized counterpart on Γ_e when a Ricker of 10 Hz and a sensor spacing of 1 m are used.

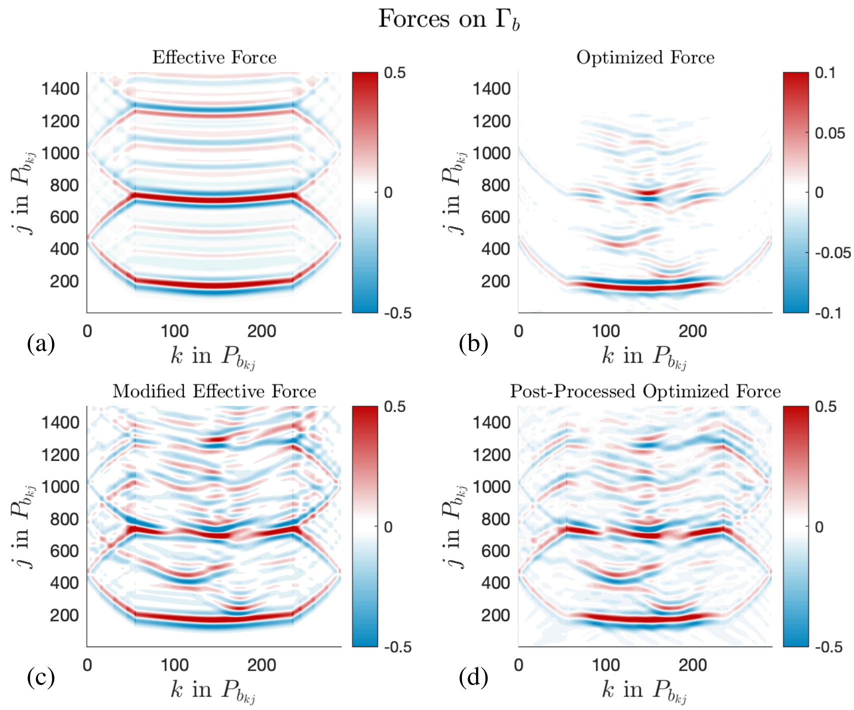

Figure 19: Example 3 - (a) Effective seismic force and (b) its final-optimized counterpart; and (c) modified effective seismic force and (d) its post-processed optimized counterpart on Γ_b when a Ricker of 10 Hz and a sensor spacing of 1 m are used.

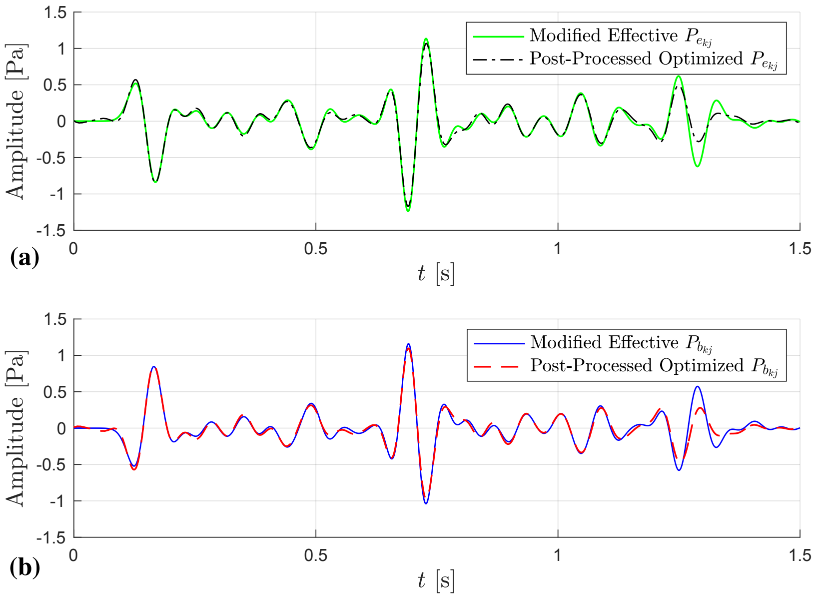

Figure 20: Example 3 - Time signals of modified effective and post-processed optimized forces at (a) x = 100 m and y = 56 m on Γ_e, and (b) x = 100 m and y = 55 m on Γ_b, when a Ricker of 10 Hz and a sensor spacing of 1 m are used.

5.4. Example 4: Assessing the performance to reconstruct ground motions with respect to the incident angle of an incoming wave

The originally-presented incident SH waves are not plane waves with specific directions. While our method is generally applicable for arbitrary types of an incident wave, our previously-shown Examples 1 to 3 considered three different point sources at different locations for demonstrations in each example: one at near surface and two at far field. Each point source radiates in all directions and contains all angles in the wavenumber space. Thus, Examples 1 to 3 generally accommodate a broad range of angles of incident waves.

The purpose of this example 4 is to evaluate the performance of the presented method on reconstructing ground motions in Ω_i with respect to the predominant incident angle of an incoming wave entering Ω_i. To this end, we consider a line array of seismic wave sources in the bottom-left part of an enlarged domain so that we mimic a strike slip on a fault line using line body force loading in the anti-plane direction. Each wave source of this line body force loading is characterized by a 10 Hz Ricker source signal. The line loading generates an inclined plane incident wave in the enlarged domain with a specific predominant angle of incidence if the material of the enlarged domain is homogeneous. Thus, this example considers a homogeneous enlarged domain with the two inclusions. The wave speeds V_{s_1}, V_{s_2}, V_{s_3}, V_{s_4}, V_{s_7}, and V_{s_8} in the previous Examples 1 to 3 are now all reset to 250 m/s (i.e., the homogeneous background material's wave speed) while V_{s_5} and V_{s_6}—800 and 1000 m/s, respectively—remain the same (i.e., the two inclusions' wave speeds).

Fig. 21(a) shows an examplary strike-slip-like line body force loading in the enlarged domain to create an incident wave of its predominant incident angle of 45°. Fig. 21(b) shows the inclined incident waves entering Ω_i with three different predominant incident angles θ (i.e., 26.57°, 45°, and 63.43°, respectively). We examine the presented method's performance to reconstruct ground motions induced by each of these three different inclined plane waves using a sensor spacing of 1 m.

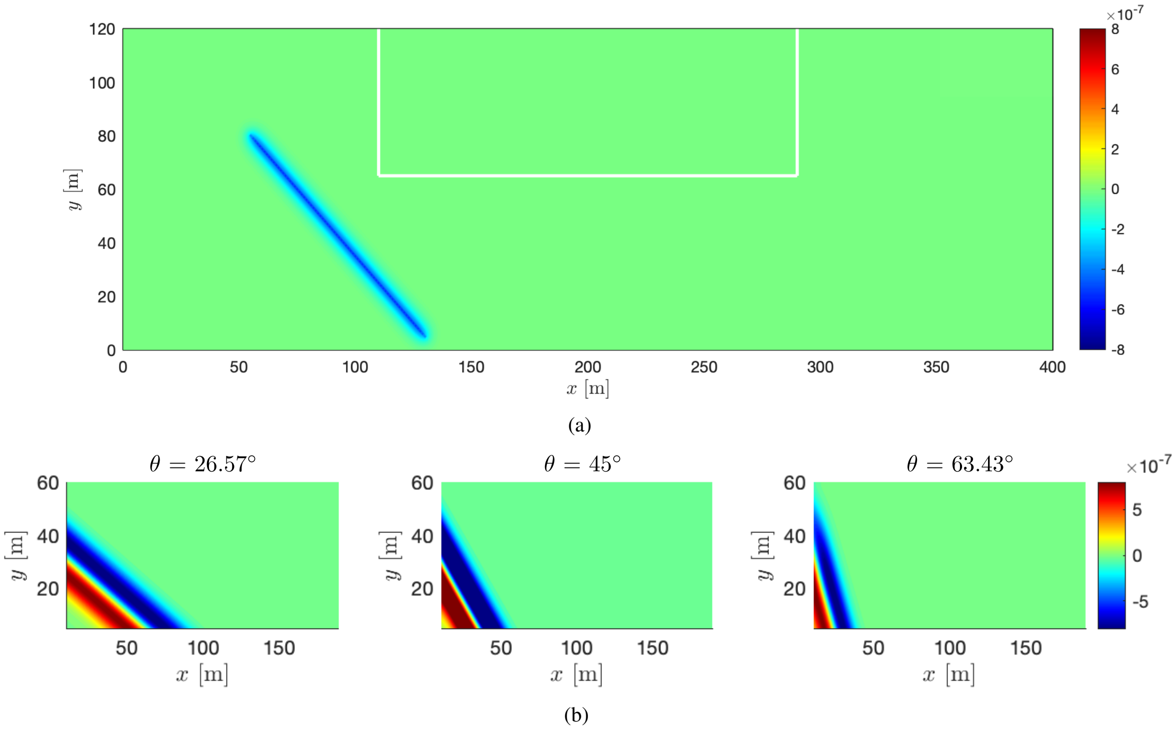

Figure 21: Example 4 - (a) An exemplary strike-slip-like line body force loading in the enlarged homogeneous background domain; (b) targeted incident waves with three different angles of incidence—26.57°, 45°, and 63.43°—entering the reduced domain.

Table 1 shows the final values of errors for each case in Example 4 and those in Example 1-3 that employed a Ricker of 10 Hz and a sensor spacing of 1 m. We note that the values of errors (i.e., $\mathcal{E}^u$ and $\mathcal{E}$) in Example 4 are of the same order of magnitude as those in Examples 1-3, indicating that the presented method is omnidirectionally applicable in terms of the incident angle of an incoming wave.

Table 1: Comparison of $\mathcal{E}^u$ and $\mathcal{E}$ obtained in Examples 1-4 when a Ricker of 10 Hz and a sensor spacing of 1 m are used.

Cases	$\mathcal{E}^u$	$\mathcal{E}$
Example 1	1.08%	15.21%
Example 2	2.94%	13.01%
Example 3	2.29%	8.23%
Example 4: θ = 26.57°	4.97%	15.80%
Example 4: θ = 45°	3.70%	7.35%
Example 4: θ = 63.43°	5.98%	16.14%

Fig. 22 shows the agreement between targeted ground motions for three different predominant angles of incidence in Ω_i at t of 0.53 s and their reconstructed counterparts.

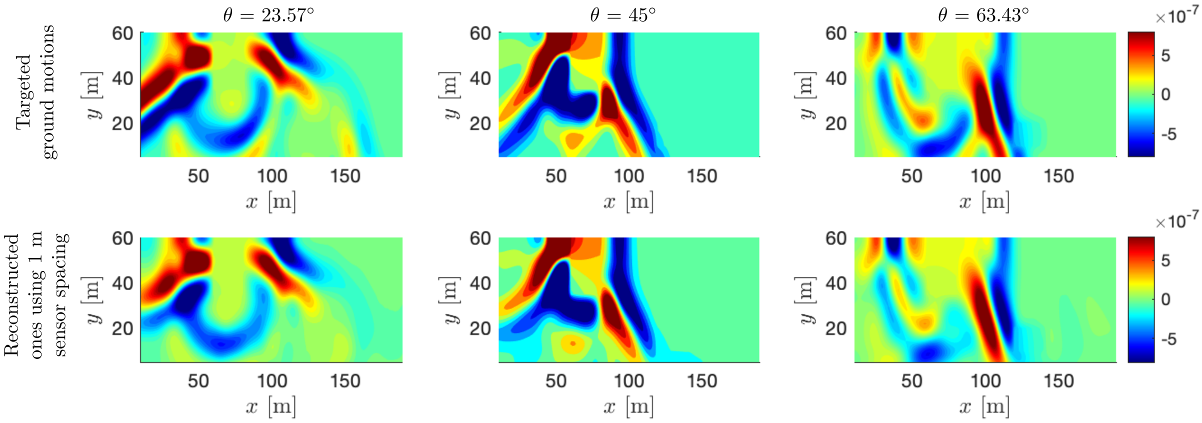

Figure 22: Example 4 - Targeted wave responses in Ω_i propagating in three different predominant angles and their reconstructed counterparts at t = 0.53 s.

Fig. 23 compares reference and optimized force vectors and their modified/post-processed counterparts on Γ_b for the case in which the incident angle of an incoming wave is 45°. Fig. 23 shows excellent agreement between the modified effective seismic force and its post-processed optimized counterpart. In addition, Fig. 24 reveals agreement between modified effective and post-processed optimized forces corresponding to the nodes on the bottom-left portion of Γ_e and Γ_b at x of 55 m and y of 56 m and 55 m, respectively, for three predominant incident angles of incoming waves.

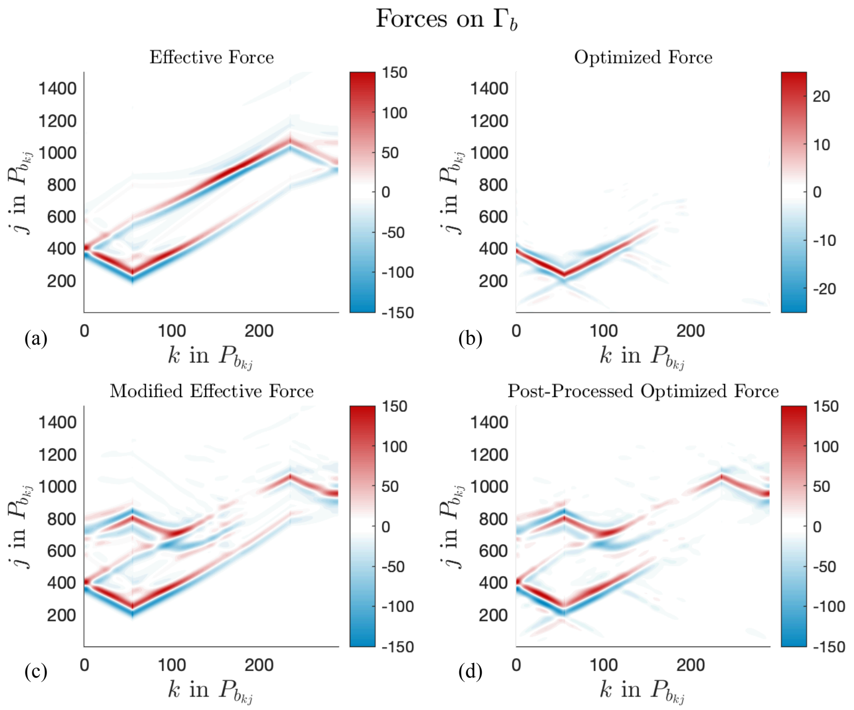

Figure 23: Example 4 - (a) Targeted effective seismic force and (b) its final-optimized counterpart; and (c) modified effective seismic force and (d) its post-processed optimized counterpart on Γ_b when the incident angle of the incoming wave is 45°.

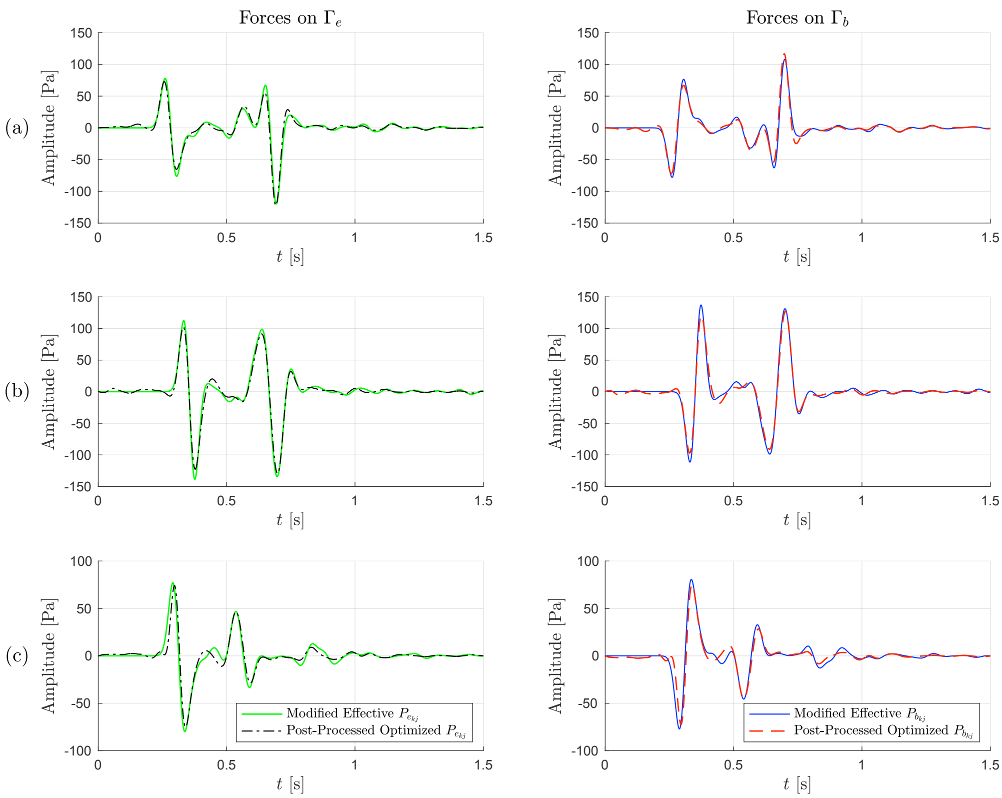

Figure 24: Example 4 - Time signals of modified effective and post-processed optimized forces at $x = 55$ m and $y = 56$ m on Γ_e and $x = 55$ m and $y = 55$ m on Γ_b when the predominant incident angle of an incoming wave is (a) 23.57°, (b) 45°, and (c) 63.43°.

5.5. *Time duration effect*

In Figs. 10, 15, and 20, the disagreement between the $\hat{\mathbf{F}}^{\text{eff}}_{\text{mod}}$ and $\hat{\mathbf{F}}^{\text{opt}}_{\text{pp}}$ is more noticeable at the later time steps (e.g., 1.2 to 1.5 s). Such a larger error at the later time is due to the fact that we cannot identify the part of $\hat{\mathbf{F}}^{\text{eff}}_{\text{mod}}$ that is attributed to the incident waves in the later time, which do not arrive at the sensors before the end of the observation duration.

Thus, the issue can be resolved simply by considering a longer observation time. We rerun the examples 1-3 with a longer duration of 3 seconds with a Ricker of 10 Hz and the sensor spacing of 1 m. Fig. 25 shows the time signals of modified effective and post-processed optimized forces on Γ_e and Γ_b at the same nodal locations discussed in Fig. 10, 15, and 20. We observe a very good agreement at 1.2 to 1.5 s.

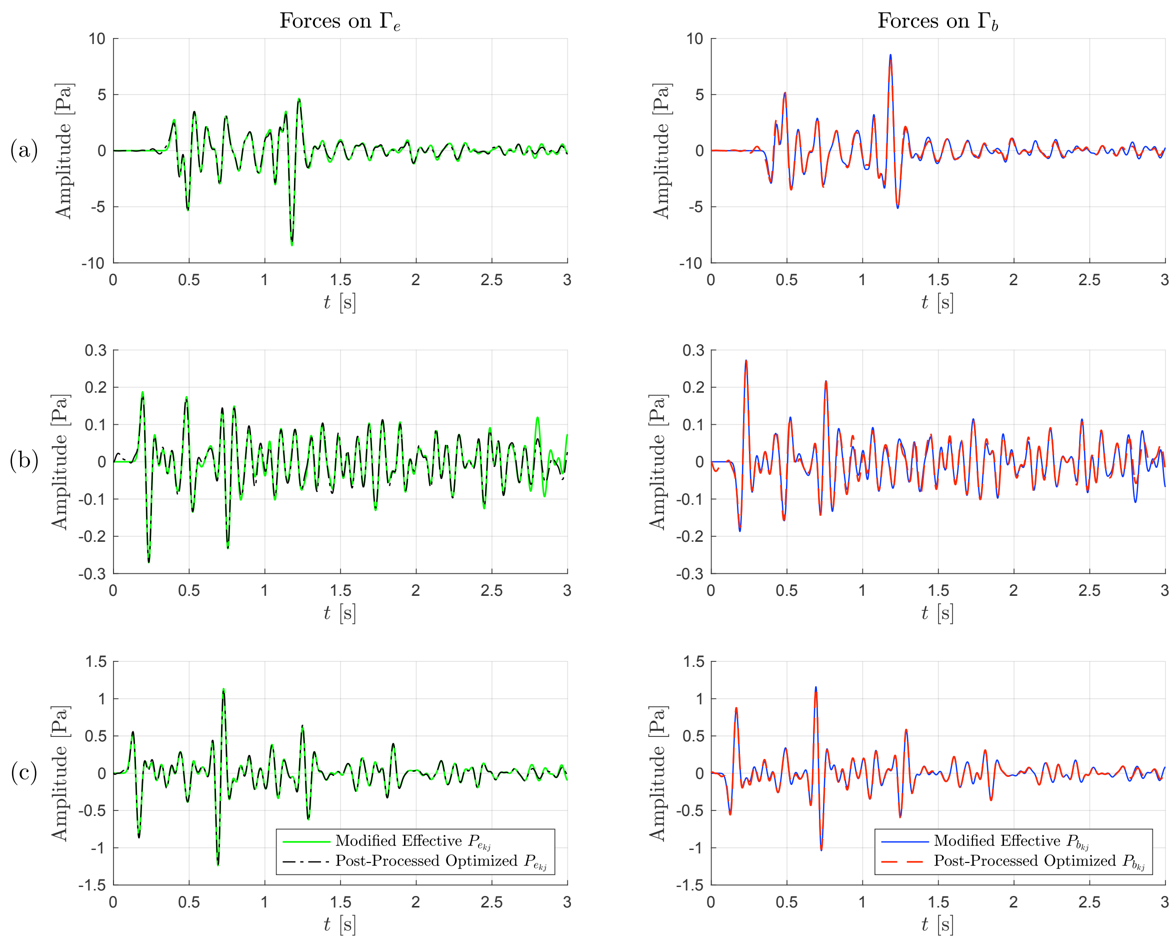

Figure 25: Time signals of modified effective and post-processed optimized forces on Γ_e and Γ_b when a Ricker of 10 Hz, a sensor spacing of 1 m, and a long observation duration (i.e., 3 seconds) are used in (a) Example 1, (b) Example 2, and (c) Example 3. The signals correspond to the same nodal locations discussed in Fig. 10, 15, and 20.

6. Conclusion

In this paper, we presented a new numerical approach for optimizing dynamic forces at virtual interfaces to reconstruct the shear wave ground motions induced by a seismic source outside of the truncated domain. An enlarged domain is utilized in the forward wave solver to model arbitrarily-incoherent incident waves that propagate into the truncated domain and to generate targeted measurement data at sensors. The optimization problem is tackled using a gradient-based minimization, where the DTO method is implemented to solve the adjoint problem and calculate the gradient of the objective functional.

The performance of the presented optimizer was numerically tested for different frequencies of the incident waves, sensor spacings on the surface, and the angles of incident waves. The numerical examples present the following insights. First, the targeted wave responses obtained from an enlarged domain can be reconstructed within the interior domain by using the optimized forces from the presented method. Second, the optimized seismic force vector may differ from its reference standard DRM counterpart while being a valid solution among other possible solutions allowed by the DRM and alternative decompositions of total field into incident and scattered fields. Third, we introduce a post-processing technique to properly compare the optimized force vector with its reference value. By post-processing the optimized body force at virtual interfaces, we can identify "modified" targeted effective seismic forces at the interfaces such that scattered wave in the exterior domain is silenced. Fourth, the presented inversion method can reconstruct the dynamic motions in a truncated domain impinged by typical seismic waves of a continuous frequency spectrum. Fifth, the presented method is omnidirectionally applicable in terms of the incident angle of an incoming wave. Lastly, we study the desired spacing of sensors to accurately reconstruct the ground motions, which depends on the dominant frequency of the incident waves.

The proposed method provides an efficient method to study the effect of a seismic event on a soil-structure system such as foundations and underground structures. As the merit of the presented inversion method, it necessitates the information of the wave speeds and dimensions of only a reduced domain. Namely, the geophysical profile of an enlarged domain or a seismic source profile outside a reduced domain do not need to be informed to the presented inversion simulator. Thus, the computational cost of the method is quite compact even though it leads to the high-fidelity reconstruction of wave response in the reduced domain. In addition, even though the dispersive properties (natural frequency, wave velocities, etc.) due to material heterogeneity or geometry of layering affect the wave motion, the presented method is effective, for any given material heterogeneity and geometry of layering of the domain, in inverting for DRM force using measurement on the surface. Namely, the presented method can be used for any depth of layers in a reduced domain, which can also be unbounded homogeneous soil.

A three-dimensional extension of this study is straightforward and will provide a computationally efficient framework in earthquake engineering by selectively modeling a near-surface domain without including the hypocenter. The proposed method could also be extended by using a more robust WABC, such as the Perfectly Matched Layer (PML) [46, 47], instead of the presented Lysmer-Kuhlemeyer WABC [34], to prevent spurious reflection at the truncated boundary, which may improve the performance of the inverse process.

Funding

This material is based upon work supported by the National Science Foundation under Awards CMMI-2044887 and CMMI-2053694. Any opinions, findings, and conclusions or recommendations expressed in this material are those of the authors and do not necessarily reflect the views of the National Science Foundation. The authors are also grateful for the support by the Faculty Research and Creative Endeavors (FRCE) Research Grant-48058 at Central Michigan University.

Availability of data and material

All data and models of the presented numerical results—e.g., MATLAB datasets (.mat format)—are available by request to the corresponding author.

Code Availability

MATLAB code (.m format) of the presented inverse modeling is available available by request to the corresponding author.

Nomenclature

Symbol	Definition
x, y, z	Horizontal, vertical, and anti-plane directions, respectively
t, T	Time and final time of J
J	Duration of the observation
$u(x, y, t)$	Displacement field of dynamic motions polarized in the z-plane
$G(x, y)$, $V_{\mathrm{s}}(x, y)$	Shear modulus and shear wave speed
$\rho(x, y)$	Mass density
Ω	Domain
Ω_i, Ω_e	Interior and exterior domain, respectively, inside and outside virtual interface
$\Gamma_{\mathrm{top}}, \Gamma_{\mathrm{bottom}}$	Top and bottom boundaries of Ω
$\Gamma_{\mathrm{right}}, \Gamma_{\mathrm{left}}$	Right and left boundaries of Ω
$\mathbf{u}(t)$	Displacement solution vector at t
$\mathbf{M}, \mathbf{K}, \mathbf{C}, \mathbf{F}$	Global mass, stiffness, and damping matrices, and global force vector
Γ_b	Inner virtual interface boundary; Inner boundary of a DRM layer
Γ_e	Outer virtual interface boundary; Outer boundary of a DRM layer
$\mathbf{F}^{\mathrm{eff}}$	Effective force vector
$\mathbf{M}_{be}^{\Omega_e}$, $\mathbf{M}_{eb}^{\Omega_e}$	Mass matrices that correspond to the nodes only in the DRM layer
$\mathbf{K}_{be}^{\Omega_e}$, $\mathbf{K}_{eb}^{\Omega_e}$	Stiffness matrices that correspond to the nodes only in the DRM layer
$\mathbf{u}^0$, $\ddot{\mathbf{u}}^0$	Free-field displacements and accelerations, respectively
$\mathbf{Q}$	Matrix comprised of the $\mathbf{M}, \mathbf{K}$, and $\mathbf{C}$ matrices, indicating the Newmark time integration
$\hat{\mathbf{u}}$	Discretization, in time and space, of $u(x, y, t)$ for all t_j
$\hat{\mathbf{F}}$	Force vector for all t_j
N	Final time step
$\hat{\mathbf{F}}^{\mathrm{opt}}$	Optimized seismic force vector
γ_{b_k}, γ_{e_k}	The k-th node on Γ_b and Γ_e, respectively
k	Numbering of the node γ_{b_k} and γ_{e_k}; k-th component in $P_{b_{kj}}$ and $P_{e_{kj}}$
j	The j-th component in $P_{b_{kj}}$ and $P_{e_{kj}}$; the j-th time step;
$P_{b_{kj}}$, $P_{e_{kj}}$	Components of $\hat{\mathbf{F}}^{\mathrm{opt}}$ corresponding to γ_{b_k} and γ_{e_k}, respectively, and t_j
$\boldsymbol{\xi}$	A set of control parameters (i.e., $P_{b_{kj}}$ and $P_{e_{kj}}$)
$\hat{\mathcal{L}}$	Discrete objective functional
$u_{\mathrm{m}}(x, y, t)$	Dynamic response induced by targeted incident waves and measured by a sensor
$\hat{\mathbf{u}}_{\mathrm{m}}$	Space-time discretization of $u_{\mathrm{m}}(x, y, t)$ for all t_j
$\mathbf{B}$	Square matrix that is zero except on the diagonals corresponding to sensors
$\hat{\mathcal{A}}$	Discrete Lagrangian functional
$\hat{\boldsymbol{\lambda}}$	Lagrange multiplier vector for all the nodes and all t_j
$\mathbf{d}$, h	Search direction vector and scalar-value step size
$\mathcal{E}^u$	Error norm between dynamic motions in Ω_i induced by incident waves and its $\hat{\mathbf{F}}^{\mathrm{opt}}$ counterpart
$\mathcal{E}$	Error norm between optimized force on a DRM layer and its targeted counterpart
$f(x, y, t)$	Ricker wavelet signal
f_c	Central frequency of the Ricker signal
$\mathbf{u}^{\mathrm{t}}$, $\mathbf{u}^{\mathrm{s}}$	Total and scattered wave field, respectively
$\hat{\mathbf{F}}_{\mathrm{mod}}^{\mathrm{eff}}$	Modified effective force vector
$\hat{\mathbf{F}}_{\mathrm{pp}}^{\mathrm{opt}}$	Post-processed optimized force vector
$\mathbf{u}^{0_{\mathrm{mod}}}$, $\ddot{\mathbf{u}}^{0_{\mathrm{mod}}}$	Modified free-field displacements and accelerations, respectively
$\hat{\mathbf{u}}_{\mathrm{pp}}$	Post-processed $\hat{\mathbf{u}}$
$\mathbf{D}$	Square matrix that is zero except on the diagonals corresponding to nodes except Ω_e

Appendix A. Brief review on DRM

Per Bielak's DRM formulation [18, 19], we subdivide a reduced domain of consideration into the following three parts: an exterior domain Ω_e, an interface Γ_b, and an interior domain Ω_i, as shown in Fig. 1. A DRM layer is delineated by the nodes on Γ_b and their neighboring exterior counterparts, on a fictitious boundary Γ_e. Per the DRM theory, an effective seismic force vector $\mathbf{F}^{\text{eff}}$ is obtained from free-field dynamic responses and computed using (A.1). We, in turn, apply $\mathbf{F}^{\text{eff}}$ on all the nodes on the DRM layer (i.e., Γ_b and Γ_e if a single, four node-element DRM layer is used as in the presented paper) so that we can effectively model incident seismic waves impinging a reduced domain as an equivalent dynamic force vector in the position of $\mathbf{F}(t)$ in (7). Namely, $\mathbf{F}(t)$ in (7) is replaced by $\mathbf{F}^{\text{eff}}$ in the following:

$$\mathbf{F}^{\text{eff}} = \begin{bmatrix} \mathbf{P}_i^{\text{eff}} \\ \mathbf{P}_b^{\text{eff}} \\ \mathbf{P}_e^{\text{eff}} \end{bmatrix} = \begin{bmatrix} 0 \\ -\mathbf{M}_{be}^{\Omega_e}\ddot{\mathbf{u}}_e^0 - \mathbf{K}_{be}^{\Omega_e}\mathbf{u}_e^0 \\ \mathbf{M}_{eb}^{\Omega_e}\ddot{\mathbf{u}}_b^0 + \mathbf{K}_{eb}^{\Omega_e}\mathbf{u}_b^0 \end{bmatrix}, \tag{A.1}$$

where the subscripts i, b, and e denote the nodes in Ω_i, Γ_b, and Ω_e; $\mathbf{M}_{be}^{\Omega_e}$, $\mathbf{M}_{eb}^{\Omega_e}$, $\mathbf{K}_{be}^{\Omega_e}$, and $\mathbf{K}_{eb}^{\Omega_e}$ are the mass and stiffness matrices that correspond to the nodes only in the DRM layer: these matrices vanish everywhere except the single layer of finite elements (i.e., DRM layer). For instance, $\mathbf{M}_{be}^{\Omega_e}$ is the partition of $\mathbf{M}^{\Omega_e}$ corresponding to the row indices of $\mathbf{u}_b$ and column indices of $\mathbf{u}_e$. Only the free-field wave responses, $\mathbf{u}^0$ and $\ddot{\mathbf{u}}^0$, at nodes of the DRM layer are needed to calculate $\mathbf{F}^{\text{eff}}$. In the presented paper, an effective nodal force vector is obtained by using free-field seismic motions ($\mathbf{u}^0$ and $\ddot{\mathbf{u}}^0$) that are obtained from the forward solver using the enlarged domain. We note that, per the DRM theory, we do not consider the wave speeds of local features, such as inclusions of V_{s_5} and V_{s_6} in the presented numerical examples, in order to obtain the free-field ground motions.

Appendix B. Modified effective force vector

The modified effective force vector $\mathbf{F}_{\text{mod}}^{\text{eff}}$ is computed as:

$$\mathbf{F}_{\text{mod}}^{\text{eff}} = \begin{bmatrix} \mathbf{P}_{\text{mod}_i}^{\text{eff}} \\ \mathbf{P}_{\text{mod}_b}^{\text{eff}} \\ \mathbf{P}_{\text{mod}_e}^{\text{eff}} \end{bmatrix} = \begin{bmatrix} 0 \\ -\mathbf{M}_{be}^{\Omega_e}\ddot{\mathbf{u}}_e^{0_{\text{mod}}} - \mathbf{K}_{be}^{\Omega_e}\mathbf{u}_e^{0_{\text{mod}}} \\ \mathbf{M}_{eb}^{\Omega_e}\ddot{\mathbf{u}}_b^{0_{\text{mod}}} + \mathbf{K}_{eb}^{\Omega_e}\mathbf{u}_b^{0_{\text{mod}}} \end{bmatrix}, \tag{B.1}$$

where $\mathbf{u}^{0_{\text{mod}}}$ and $\ddot{\mathbf{u}}^{0_{\text{mod}}}$ are the modified free-field displacements and accelerations, respectively. Namely, the wave speeds of local features in the enlarged domain (i.e., V_{s_5} and V_{s_6} in the numerical examples) are considered in the forward wave solver when we obtain the modified free-field wave motions. Therefore, solving (8) using (B.1) leads the wave response in the exterior domain to vanish, while solving (8) using (A.1) leads that not to vanish but be equal to the scattered field from local features.

References

[1] L. Mejia, E. Dawson, Earthquake deconvolution for FLAC, FLAC and Numerical (2006).

[2] M. K. Poul, A. Zerva, Efficient time-domain deconvolution of seismic ground motions using the equivalent-linear method for soil-structure interaction analyses, Soil Dynamics and Earthquake Engineering 112 (2018) 138 – 151. URL: http://www.sciencedirect.com/science/article/pii/S0267726117305742. doi:https://doi.org/10.1016/j.soildyn.2018.04.032.

[3] M. K. Poul, A. Zerva, Nonlinear dynamic response of concrete gravity dams considering the deconvolution process, Soil Dynamics and Earthquake Engineering 109 (2018) 324 – 338. URL: http://www.sciencedirect.com/science/article/pii/S0267726117308825. doi:https://doi.org/10.1016/j.soildyn.2018.03.025.

[4] J. A. A. Mena, B. Jeremic, 6C vs 1C Earthquake Soil Structure Interaction (ESSI) for Nuclear Power Plants (NPPs), 2015. URL: http://sokocalo.engr.ucdavis.edu/ jeremic/6D_vs_1D_ESSI_for_NPPs/.

[5] V. Akcelik, G. Biros, O. Ghattas, Parallel multiscale Gauss-Newton-Krylov methods for inverse wave propagation, in: Supercomputing, ACM/IEEE 2002 Conference, IEEE, 2002, pp. 41–41.

[6] A. Askan, V. Akcelik, J. Bielak, O. Ghattas, Full waveform inversion for seismic velocity and anelastic losses in heterogeneous structures, Bulletin of the Seismological Society of America 97 (2007) 1990–2008. doi:10.1785/0120070079.

[7] A. Askan, J. Bielak, Full anelastic waveform tomography including model uncertainty, Bulletin of the Seismological Society of America 98 (2008) 2975–2989. doi:10.1785/0120080138.

[8] A. Askan, V. Akcelik, J. Bielak, O. Ghattas, Parameter sensitivity analysis of a nonlinear least-squares optimization-based anelastic full waveform inversion method, Comptes Rendus Mécanique 338 (2010) 364 – 376. doi:https://doi.org/10.1016/j.crme.2010.07.002, inverse problems.

[9] C. Jeong, S.-W. Na, L. F. Kallivokas, Near-surface localization and shape identification of a scatterer embedded in a halfplane using scalar waves, Journal of Computational Acoustics 17 (2009) 277–308.

[10] J. W. Kang, L. F. Kallivokas, The inverse medium problem in 1D PML-truncated heterogeneous semi-infinite domains, Inverse Problems in Science and Engineering 18 (2010) 759–786. doi:10.1080/17415977.2010.492510.

[11] K. T. Tran, M. McVay, Site characterization using Gauss-Newton inversion of 2-D full seismic waveform in the time domain, Soil Dynamics and Earthquake Engineering 43 (2012) 16–24. URL: https://linkinghub.elsevier.com/retrieve/pii/S0267726112001613. doi:10.1016/j.soildyn.2012.07.004.

[12] A. Fathi, L. F. Kallivokas, B. Poursartip, Full-waveform inversion in three-dimensional PML-truncated elastic media, Computer Methods in Applied Mechanics and Engineering 296 (2015) 39–72.

[13] A. Fathi, B. Poursartip, K. H. Stokoe II, L. F. Kallivokas, Three-dimensional P-and S-wave velocity profiling of geotechnical sites using full-waveform inversion driven by field data, Soil Dynamics and Earthquake Engineering 87 (2016) 63–81. URL: http://www.sciencedirect.com/science/article/pii/S0267726116300148.

[14] A. Pakravan, J. W. Kang, C. M. Newtson, A Gauss-Newton full-waveform inversion for material profile reconstruction in viscoelastic semi-infinite solid media, Inverse Problems in Science and Engineering 24 (2016) 393–421. URL: http://dx.doi.org/10.1080/17415977.2015.1046861. doi:10.1080/17415977.2015.1046861.

[15] C. Jeong, E. E. Seylabi, Seismic input motion identification in a heterogeneous halfspace, Journal of Engineering Mechanics 144 (2018) 04018070. doi:10.1061/(ASCE)EM.1943-7889.0001495.

[16] B. P. Guidio, C. Jeong, Full-waveform inversion of incoherent dynamic traction in a bounded 2D domain of scalar wave motions, Journal of Engineering Mechanics 147 (2021) 04021010. doi:10.1061/(ASCE)EM.1943-7889.0001909.

[17] B. Guidio, B. Jeremić, L. Guidio, C. Jeong, Passive seismic inversion of SH wave input motions in a truncated domain, Soil Dynamics and Earthquake Engineering 158 (2022) 107263. doi:https://doi.org/10.1016/j.soildyn.2022.107263.

[18] J. Bielak, K. Loukakis, Y. Hisada, C. Yoshimura, Domain reduction method for three-dimensional earthquake modeling in localized regions, Part I: Theory, Bulletin of the Seismological Society of America 93 (2003) 817–824.

[19] C. Yoshimura, J. Bielak, Y. Hisada, A. Fernández, Domain reduction method for three-dimensional earthquake modeling in localized regions, part II: Verification and applications, Bulletin of the Seismological Society of America 93 (2003) 825–841.

[20] B. Jeremić, G. Jie, M. Preisig, N. Tafazzoli, Time domain simulation of soil–foundation–structure interaction in non-uniform soils, Earthquake Engineering & Structural Dynamics 38 (2009) 699–718.

[21] B. Jeremić, N. Tafazzoli, T. Ancheta, N. Orbović, A. Blahoianu, Seismic behavior of NPP structures subjected to realistic 3D, inclined seismic motions, in variable layered soil/rock, on surface or embedded foundations, Nuclear Engineering and Design 265 (2013) 85–94.

[22] Y. Isbiliroglu, R. Taborda, J. Bielak, Coupled soil-structure interaction effects of building clusters during earthquakes, Earthquake Spectra 31 (2015) 463–500.

[23] B. Poursartip, A. Fathi, L. F. Kallivokas, Seismic wave amplification by topographic features: A parametric study, Soil Dynamics and Earthquake Engineering 92 (2017) 503–527. URL: http://www.sciencedirect.com/science/article/pii/S0267726116304559. doi:10.1016/j.soildyn.2016.10.031.

[24] J. A. Abell, N. Orbović, D. B. McCallen, B. Jeremic, Earthquake soil-structure interaction of nuclear power plants, differences in response to 3-D, 3× 1-D, and 1-D excitations, Earthquake Engineering & Structural Dynamics 47 (2018) 1478–1495.

[25] B. Poursartip, L. F. Kallivokas, Model dimensionality effects on the amplification of seismic waves, Soil Dynamics and Earthquake Engineering 113 (2018) 572–592. URL: https://www.sciencedirect.com/science/article/pii/S0267726117309570. doi:https://doi.org/10.1016/j.soildyn.2018.06.012.

[26] K. Kanellopoulos, B. Jeremic, I. Anastasopoulos, B. Stojadinovic, Use of the domain reduction method to simulate the seismic response of an existing structure protected by resonating unit cell metamaterials, in: EURODYN 2020 23-26 November 2020, Athens, Greece XI International Conference on Structural Dynamics. Proceedings, volume 19985, European Association for Structural Dynamics (EASD), 2020, pp. 2926–2938.

[27] D. Kusanovic, E. Seylabi, A. Kottke, D. Asimaki, SEISMO-VLAB: A parallel, object oriented virtual lab for mesoscale seismic wave propagation problems, in: The USSD Conference and Exhibition, 2020, pp. 97–104.

[28] L. Zhang, J.-T. Wang, Y.-J. Xu, C.-H. He, C.-H. Zhang, A procedure for 3D seismic simulation from rupture to structures by coupling SEM and FEM, Bulletin of the Seismological Society of America 110 (2020) 1134–1148.
[29] E. Esmaeilzadeh Seylabi, D. Restrepo, R. Taborda, D. Asimaki, Deterministic ground motion simulations with shallow crust nonlinearity at garner valley in southern california, Earthquake Engineering & Structural Dynamics 50 (2021) 43–59.
[30] S. Sica, A. D. Russo, Seismic response of large earth dams in near-source areas, Computers and Geotechnics 132 (2021) 103807.
[31] H. Wang, H. Yang, Y. Feng, B. Jeremić, Modeling and simulation of earthquake soil structure interaction excited by inclined seismic waves, Soil Dynamics and Earthquake Engineering 146 (2021) 106720.
[32] W. Zhang, E. Taciroglu, 3D time-domain nonlinear analysis of soil-structure systems subjected to obliquely incident SV waves in layered soil media, Earthquake Engineering & Structural Dynamics 50 (2021) 2156–2173.
[33] H. Goh, A. Alù, Nonlocal scatterer for compact wave-based analog computing, Phys. Rev. Lett. 128 (2022) 073201. doi:10.1103/PhysRevLett.128.073201.
[34] J. Lysmer, R. L. Kuhlemeyer, Finite dynamic model for infinite media, Journal of Engineering Mechanics Division, ASCE 95 (1969) 859–877.
[35] N. M. Newmark, A method of computation for structural dynamics, in: Proc. ASCE, volume 85, 1959, pp. 67–94.
[36] P. M. Karve, S. Kucukcoban, L. F. Kallivokas, On an inverse source problem for enhanced oil recovery by wave motion maximization in reservoirs, Computational Geosciences 19 (2014) 233–256.
[37] T. Walsh, W. Aquino, M. Ross, Source Identification in Acoustics and Structural Mechanics using SIERRA/SD, Technical Report, Sandia National Laboratories, 2013. URL: `https://prod-ng.sandia.gov/techlib-noauth/access-control.cgi/2013/132689.pdf`.
[38] J. M. Roesset, D.-W. Chang, I. Stokoe, H. Kenneth, M. Aouad, Modulus and thickness of the pavement surface layer from sasw tests, Transportation Research Record (1990).
[39] B. A. Luke, K. H. Stokoe II, Application of SASW Method Underwater, Journal of Geotechnical and Geoenvironmental Engineering 124 (1998) 523–531. doi:10.1061/(ASCE)1090-0241(1998)124:6(523).
[40] L. T. Brown, D. M. Boore, K. H. Stokoe, Comparison of shear-wave slowness profiles at 10 strong-motion sites from noninvasive SASW measurements and measurements made in boreholes, Bulletin of the Seismological Society of America 92 (2002) 3116–3133.
[41] B. R. Cox, D. P. Teague, Layering ratios: a systematic approach to the inversion of surface wave data in the absence of a priori information, Geophysical Journal International 207 (2016) 422–438.
[42] D. P. Teague, B. R. Cox, E. M. Rathje, Measured vs. predicted site response at the Garner Valley Downhole Array considering shear wave velocity uncertainty from borehole and surface wave methods, Soil Dynamics and Earthquake Engineering 113 (2018) 339–355.
[43] C. B. Park, R. D. Miller, J. Xia, Multichannel analysis of surface waves, Geophysics 64 (1999) 800–808.
[44] S. Rahimi, C. M. Wood, A. K. Himel, Application of microtremor horizontal to vertical spectra ratio (MHVSR) and multichannel analysis of surface wave (MASW) for shallow bedrock mapping for transportation projects, in: Geo-Congress 2020: Modeling, Geomaterials, and Site Characterization, American Society of Civil Engineers Reston, VA, 2020, pp. 622–632.
[45] L. Kallivokas, A. Fathi, S. Kucukcoban, K. Stokoe, J. Bielak, O. Ghattas, Site characterization using full waveform inversion, Soil Dynamics and Earthquake Engineering 47 (2013) 62–82. SI: José Manuel Roësset.
[46] A. Fathi, B. Poursartip, L. F. Kallivokas, Time-domain hybrid formulations for wave simulations in three-dimensional PML-truncated heterogeneous media, International Journal for Numerical Methods in Engineering 101 (2015) 165–198.
[47] S. François, H. Goh, L. F. Kallivokas, Non-convolutional second-order complex-frequency-shifted perfectly matched layers for transient elastic wave propagation, Computer Methods in Applied Mechanics and Engineering 377 (2021) 113704. URL: `https://www.sciencedirect.com/science/article/pii/S0045782521000402`. doi:https://doi.org/10.1016/j.cma.2021.113704.